The International Journal of

ENERGY & ENGINEERING SCIENCES

Table of Contents

USE OF SEWAGE SLUDGE ASH IN SOIL IMPROVEMENT

Süleyman Demir
Kilis 7 Aralık University
suleymandemir@kilis.edu.tr

Ali Fırat Cabalar
Gaziantep University
cabalar@gantep.edu.tr

ABSTRACT: The Sewage sludge ash (SSA) was added to the clay with the mixture ratio of 0% 10%, 20%, 30%. The SSA used in the research is a product generated during the combustion of sewage sludge in Gaziantep municipal wastewater treatment plant. The clay employed in the experimental studies was obtained from the Gaziantep University of Gaziantep campus. An intensive series of fall cone tests (FCT) were performed on the clay-SSA mixtures. The results indicated that the liquid limit estimates and undrained shear strength values of the mixtures were increased by the addition of SSA contents.

Keywords: Sewage sludge ash, fall cone, undrained shear strength.

INTRODUCTION

Sludge waste materials are one of the waste materials which many researches are available (Epstein, 1975; Moo and Zimmie,1996; Al-Sharif et al., 2000; Lo at al., 2002; Ona and Osario, 2006; Deng et al., 2007; Lin et al., 2007; Chen and Lin, 2009). Epstein (1975) mixed SSA with silty soil reviewed effect of SSA on the water retention, hydraulic conductivity, and aggregate stability in periodic time. The results indicated that additional of SSA increased the water retention, the hydraulic conductivity, and the stable aggregates. Some researchers claimed that some specification of sludges such as permeability similar to clays therefore sludges can be used for construction of barrier layers in landfill final covers (Moo and Zimmie, 1996; Lo et al., 2002). Moo and Zimmie (1996) found that Paper mill sludges have a high compressibility, and high Atterberg limits. Lin et al., (2007) use sludge/hydrated lime additive ratio in cohesive soil with 0%, 2%, 4%, 8%, 16%. The researchers rewieved the pH values, atterberg limits, compaction tests, unconfined compressive strength tests, swelling potential, CBR, and shear values of mixing. The results indicated that sewage sludge/hydrated lime decreased the plasticity index but increased CBR values, triaxial shear strength, unconfined compression strength, and shear strength. Lin et al. (2005) mixed clay and sludge ash indicated that the SSA increased unconfined compressive strength, CBR value, shear strength cohesion and the sludge ash additive reduce swelling and internal friction of the soil. Chen and Lin (2009) carried out a similar research but mixed clay with sludge/cement ratio.

The result showed that CBR, unconfined compressive strength, triaxial compression and swelling properties of soil improved with the sludge/cement additions. Deng et al., 2007 found that dry unit weight, unconfined compressive strength, CBR values, cohesive parameter and shear strength increase with sludge ash added. Al-Sharif et al. (2000) used burned sludge ash as a soil stabilizing agent at 550 °C concluded that sludge could use as a soil stabilizing including dry density, unconfined compression test, swell pressure. In addition sludge could increase the resistance against erosion (Ona and Osorio, 2006).

As a result, SSA which is one of the waste products could improve geotechnical some geotechnical properties. Therefore, in this study, The SSA were added to the clay by dry weigth with the mixture ratio of 0%, 10%, 20%, 30%. Clay used in the study collected from the Gaziantep university campus, SSA collected from Gaziantep municipal wastewater treatment plant. In the study FCT were conducted and how the SSA change of geotechnical properties of clayey soils was investigated.

MATERIALS AND METHOD

The SSA used in the research is a by-product generated during the combustion of sewage sludge in Gaziantep municipal wastewater treatment plant. The scanning elektron microscope (SEM) picture of the SSA is shown in Figure 1.
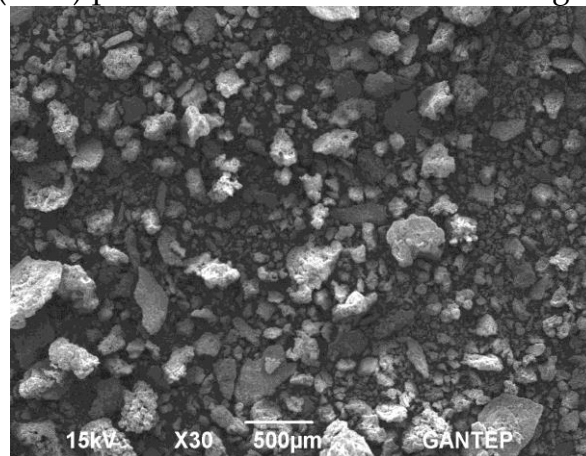
Fig 1. SEM picture for the SSA used the experimental study
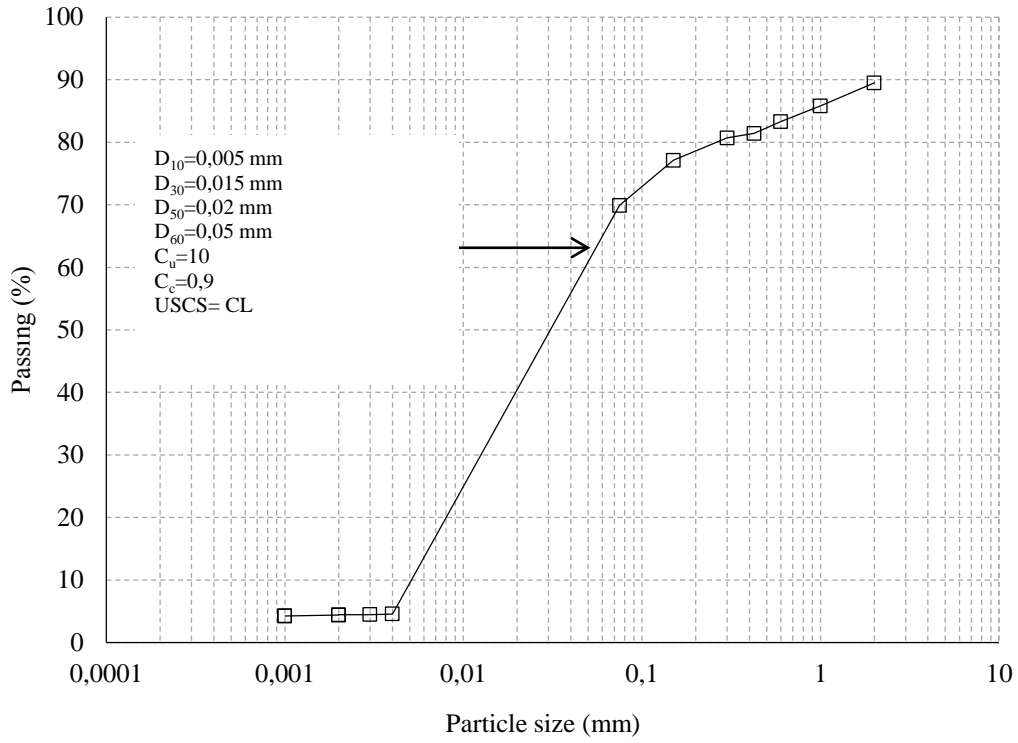
Fig 2. Particle size distributions for the clay used the experimental study

The clay samples used in this study were collected from Gaziantep university campus. The results of sieve analysis of clay are shown in Figure 2. The mixtures were waited in the oven for 24 hours at 105 °C before experimental study. The dry mixtures were prepared by calculated the desired SSA and clay in percent by dry weight and mixed in dry state until a homogeneous distribution was observed. FCT were carried out according to BS 1377 using a British fall cone apparatus having a 30° cone and weighing 0.785 N. It has been indicated that the fall cone testing is a strength measuring device and Hansbo (1957) suggested that undrained shear strength (s_u) can be found by using Equations 1.

$$s_u = k \frac{mg}{d^2}$$ (1)

where, m is the mass of cone, g is the gravitational acceleration, k is a constant, which changes based on the angle of the cone and it is found to be 0.85 for the 30° British cone (Wood, 1985), d is a penetration of cone into soil.

RESULTS AND FINDINGS

Variations of FCT penetration and the water content for each of the mixtures are shown in Fig. 3. As can be seen from Fig. 3, there is an approximately linear relationship between the cone penetration and the water content. As the water content increase the cone penetration values are increase for each mixture. In addition, at a given water content as the SSA content increases, the penetration of mixtures decreased which means SSA increased the resistance of penetration. From

FCT results liquid limit values generally obtained by water content corresponding 20 mm cone penetration (Cabalar and Mustafa, 2015). The liquid limit results are shown in Fig. 4. With the increase of the SSA liquid limit values were increased. While the liquid limit of clay was 30, with the addition of 20% and 30% SSA, the estimated value of liquid limit increased at a rate of 33.33% and 46.66% respectively. s_u values from FCT were found from equation 1 and are showed a relation with water content (Fig.5. As can be seen from Fig.4 as increase water content for each mixing the s_u values are decrease. s_u values increase with the increase of SSA value at same water content. The 10% and 20% SSA content with the following values of 40% water content, s_u values of 10% SSA content was 0.3 kPa while s_u with 20% SSA was 0,8 kPa which mean increased at the rate of 166%. This behaviour could attiributed to increase suction stress with the SSA addition as Veeresh et al., 2003 and Epstein, 1975 concluded. Suction stress could increase penetration resistance and undrained shear strength (Likos and Jaafar, 2014). Similar results were found by Lin et al. (2005) who indicated that SSA increased triaxial shear strength.
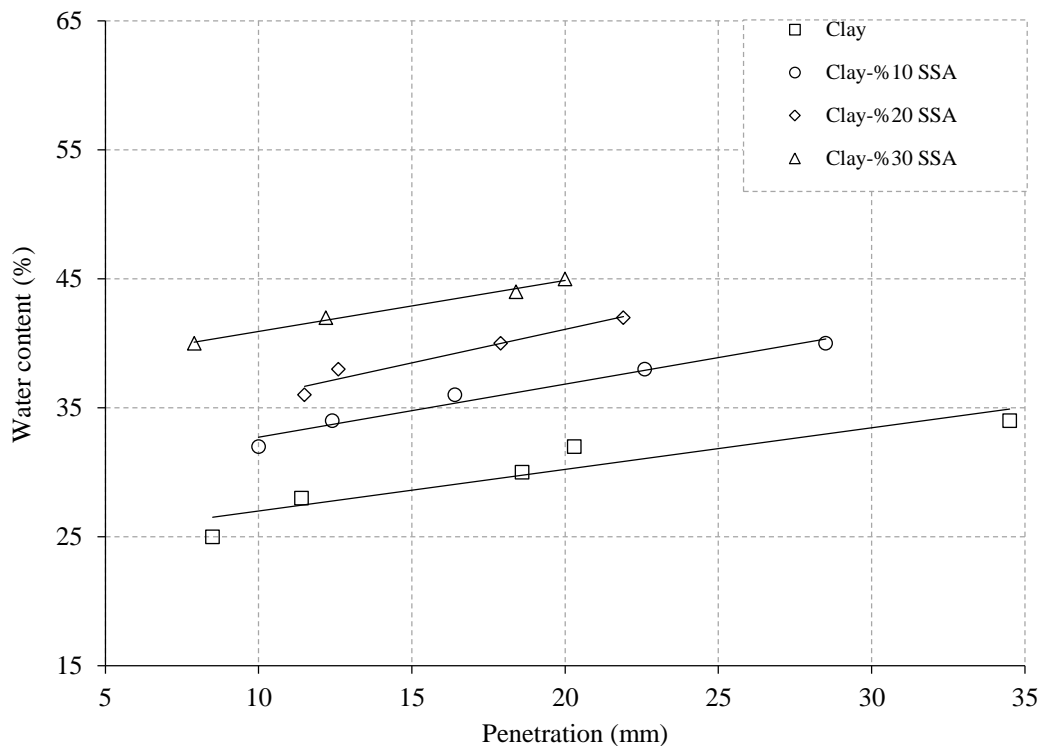
Fig 3. Variation of cone penetration with water content for clay with various SSA content
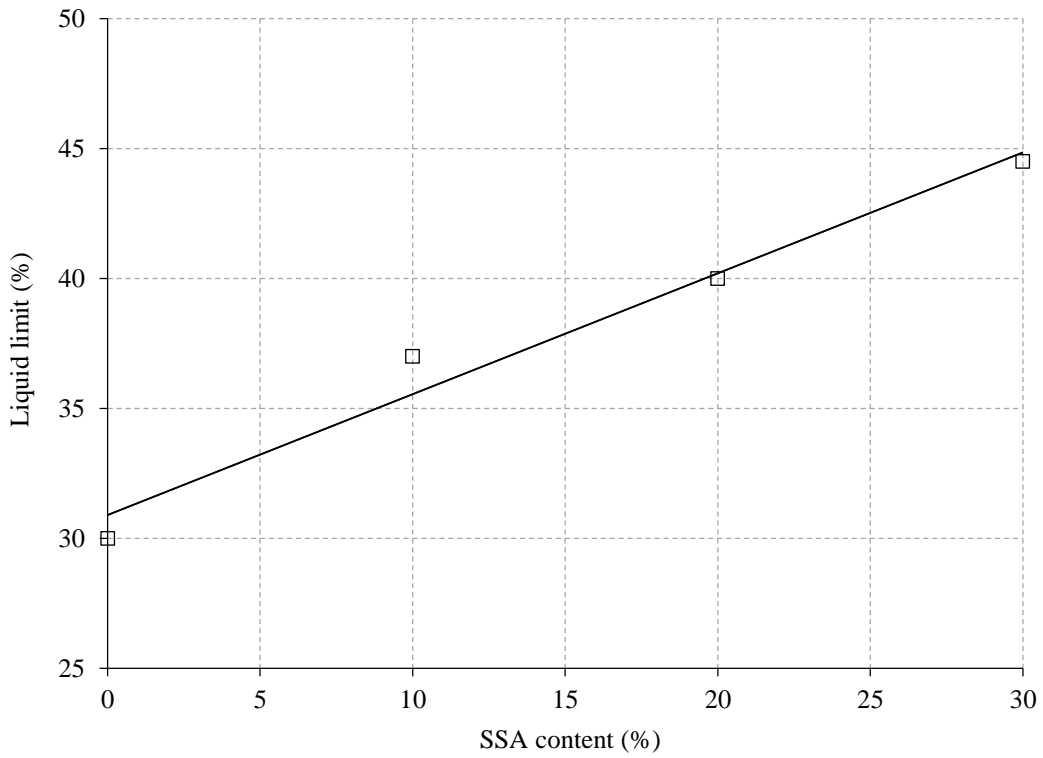
Fig 4. Liquid limit of clay with various SSA content
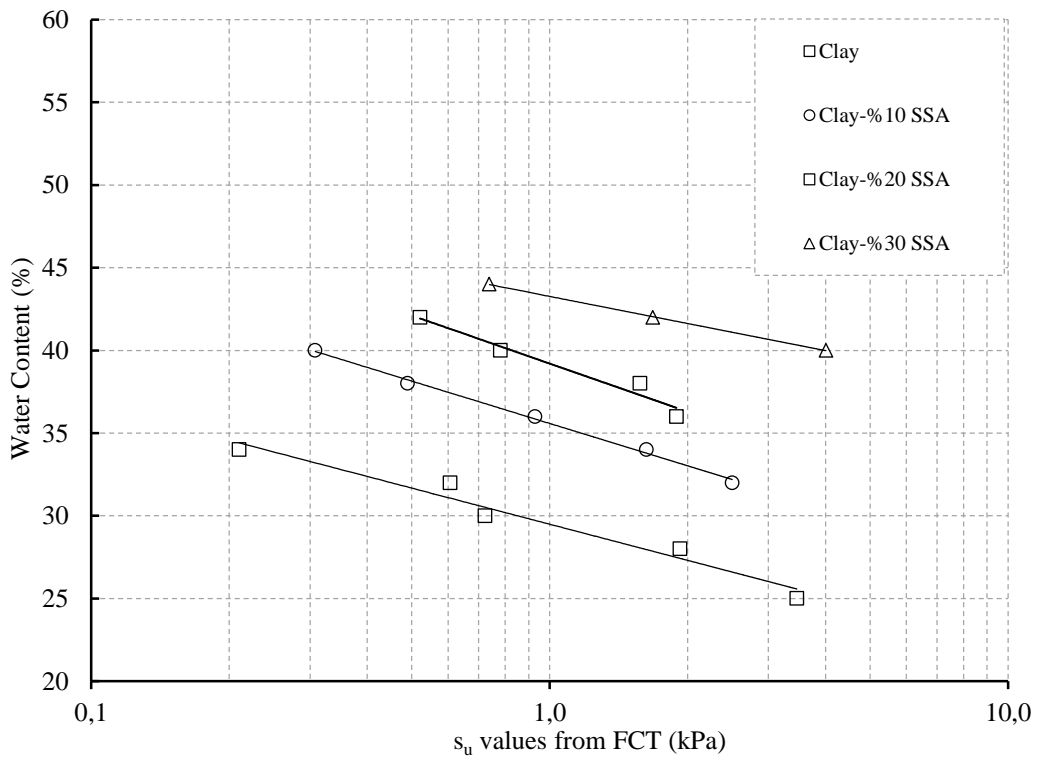
Fig 5. Relationship between undrained shear strength and water content for the clay
with various SSA content

CONCLUSIONS

The presence of SSA affected liquid limit and undrained shear strength characteristics of the clayey soil. SSA significantly increased the values of liquid limit of clay soils. Falcone penetration and undrained shear strength values with water content showed a linear behavior in all mixtures. The s_u values were observed an increase with the SSA content.

REFERENCES

Chen, L., & Lin, D. F. (2009). Stabilization treatment of soft subgrade soil by sewage sludge ash and cement. Journal of Hazardous Materials, 162(1), 321-327

De Oña, J., & Osorio, F. (2006). Application of sludge from urban wastewater treatment plants in road's embankments. Journal of Hazardous Materials,131(1), 37-45

Lin, D. F., Lin, K. L., & Luo, H. L. (2007). A comparison between sludge ash and fly ash on the improvement in soft soil. Journal of the Air & Waste Management Association, 57(1), 59-64.

Cabalar, A. F., & Mustafa, W. S. (2015). Fall cone tests on clay–sand mixtures. Engineering Geology, 192, 154-165.

Epstein, E. (1975). Effect of sewage sludge on some soil physical properties. Journal of Environmental Quality, 4(1), 139-142.

Moo-Young, H. K., & Zimmie, T. F. (1996). Geotechnical properties of paper mill sludges for use in landfill covers. Journal of Geotechnical Engineering, 122(9), 768-775.

Hansbo, S., 1957. A new approach to the determination of the shear strength of clay by the fall-cone test. R. Swedish Geotech. Inst. Proc. No. 14 (7 ± 47).

Likos, W. J., & Jaafar, R. (2014). Laboratory fall cone testing of unsaturated sand. Journal of Geotechnical and Geoenvironmental Engineering, 140(8).

Lin, D. F., Luo, H. L., Hsiao, D. H., & Yang, C. C. (2005). The effects of sludge ash on the strength of soft subgrade soil. Journal of the Chinese Institute of Environmental Engineering, 15(1), 1-10.

Lin, D. F., Lin, K. L., Hung, M. J., & Luo, H. L. (2007). Sludge ash/hydrated lime on the geotechnical properties of soft soil. Journal of Hazardous Materials,145(1), 58-64

Lo, I. M., Zhou, W. W., & Lee, K. M. (2002). Geotechnical characterization of dewatered sewage sludge for landfill disposal. Canadian Geotechnical Journal,39(5), 1139-1149.

Sharif, A, Munjed, M.; Attom, M.F. (2000). The Use of Burned Sludge as a New Soil Stabilizing Agent. ASCE National Conference on Environmental and Pipeline Engineering, Kansas City, MO, July 23–26; 378-388

Veeresh, H., Tripathy, S., Chaudhuri, D., Ghosh, B., Hart, B., & Powell, M. (2003). Changes in physical and chemical properties of three soil types in India as a result of amendment with fly ash and sewage sludge. Environmental Earth Sciences, 43(5), 513.

Wood, D.M. (1985). Some fall cone tests. Geotechnique 35 (1), 64–68.

DESIGN OF MULTIBAND ANTENNAS LOADED WITH ARRAYS OF CSRR AND CIRCULAR HEAD DUMBBELL STRUCTURE

Amer Hasan AL-Shathr[1], Gölge Ögücü Yetkin[1]
[1]University of Gaziantep, Electrical-Electronics Eng. Dept., Gaziantep, Turkey
amirshather@gmail.com, ogucu@gantep.edu.tr

ABSTRACT: This research focus on two aims, the first one is design a multi-band rectangular Microstrip Patch Antenna with spacious bandwidth by using Complementary Split Ring Resonator (CSRR) beside the Rectangular Ruler Patches (RRPs) and the second is improvement the performance and bandwidth for WiMAX and GPS applications by using Circular Head Dumbbell Structure CHDS beside Circular Ring Patches CRPs. A patch antenna is designed and simulated for 4.66 and 5.61 GHz. Two substrates of FR-4 lossy are utilized with 4.3 dielectric constant, 1.4mm and 0.2mm thickness. The shape used for conventional patch antenna is rectangular with a central feed source. For metamaterial antenna CSRR and CHDS are used. RRPs and CRPs that are used with metamaterial behave like Reactive Impedance surface RIS. The conventional antenna operates at a frequency band of 4.66 GHz and 5.61 GHz, while the designed antenna with CSRR generates four wide band resonant modes at 4.36, 4.7, 5.6 and 5.9 GHz, therefore considered as a multi-use antenna. CHDS appears fixed behavior with all RIS used to confirm its importance in WiMAX and GPS applications. Computer Simulation Technology CST EM simulator is used for this survey.

Keywords: CSRR, RRPs, CHDS, CRPs, CST.

INTRODUCTION

It has become known in wireless communications that microstrip patch antenna has the priority in many usages because of the unique features such simple in manufacturing, tiny size, lower cost than others, light weight, has the ability to integrate with integrated microwave circuits [1]. The first microstrip patch antenna was formed as early as 1970 [2]. The first proposal to design microstrip antenna was by Deschamps in 1953, where gained considerable attention later [3]. There are certain techniques used to feed the microstrip patch antenna [4], like microstrip line feed, probe feed, proximity feed, and aperture feed. The focus on the use of metamaterial in recent time has had a clear effect in improving the microstrip antenna function [2-3]. CSRR is a type of metamaterial that has a negative dielectric constant ε [5], also became very diffuse issue in order to realize a multi-band microstrip antenna [6]-[7]. Speedy development of the wireless communications has made multi-band frequency a necessity for many applications and functions. In addition, the equipment that has this capacity can perform multiple functions at the same time, which may include data transmit, video, audio, radio and so on [8]. In a multi-band antenna, each part operates in a certain range and its gain is below

average. The antenna that has circular polarization allows the transmission of steady data without relying on the guidance of the transmitter or receiver, so it is extremely appropriate for communicable equipment and mobile devices. When there are two vertical patterns excited on the antenna in order to output circular polarization which is required for GPS, the broad E-plane patterns are also orthogonally guided in space, supplying broad covering in both main planes. That produces almost a hemispherical pattern, which is perfect for use in GPS, where multiple satellites are in demand to accuracy locate the site [9]. For the purpose of realizing WiMAX and WLAN applications there have been a number of designs that suggest the operation of antenna with dual or multi-band characteristics. Operating frequencies of WLAN are (2.4-2.484) GHz, (5.15-5.35) GHz and (5.725-5.825) GHz and WiMAX (2.5-2.69) GHz, (3.4-3.69) GHz and (5.25-5.85) GHz [10-11].There are many proposals, techniques, and structures adopted to obtain a dual-band or multi-band antenna for WiMAX and WLAN applications such as the ring patch antenna [12-13], the monopole antennas [14], the slot antennas [15]. In this survey array of CSRR and CHDS with RRPs and CRPs as RIS were used in order to achieve multi-band antenna with circular polarization through excitation of two perpendicular polarization modes together at the same time with a 90 ° phase difference depending on [9]. At the end there will also be a study of CHDS behavior and its importance for WiMAX and GPS applications depending on dB.

CONFIGURATION AND DESIGNING PRINCIPLES

The geometrical design of conventional antenna with array 3x3 of CSRR and array of 15x1 RRPs will be shown in Fig1, where
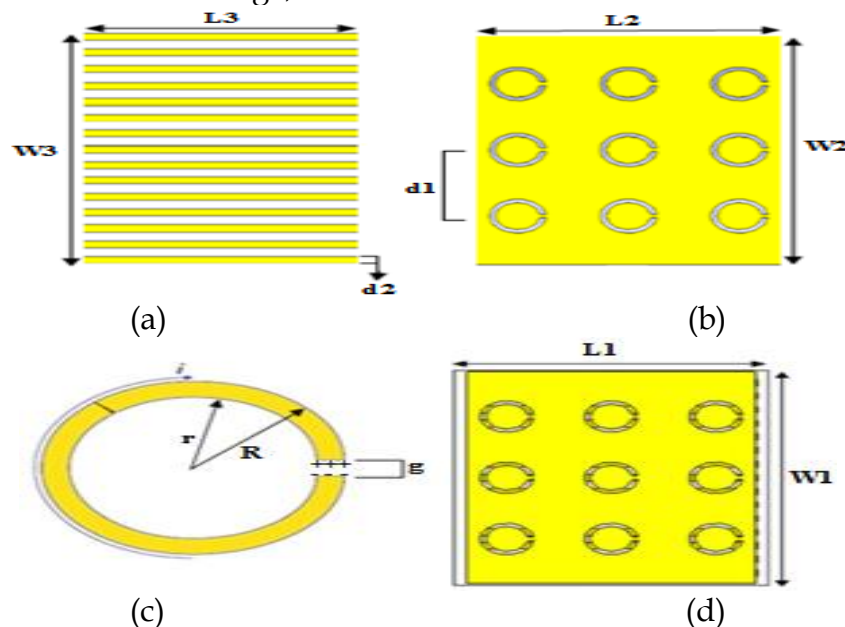
Fig.1. Structural Parts of Multi-Band Antenna: (a) RRPS, (b) CSRR, (c) Single Circular Ring of CSRR, (d) Integrated Antenna.

For CSRR the average loop length is:

$$L = 2\pi \times ((r + R)/2) - g$$

Frequency calculates by:

f = (C/(2L√ε)) Hz
Resonant frequency:
fo = (1/(2π√LC)) Hz
Where L&C represent the inductance and capacitance
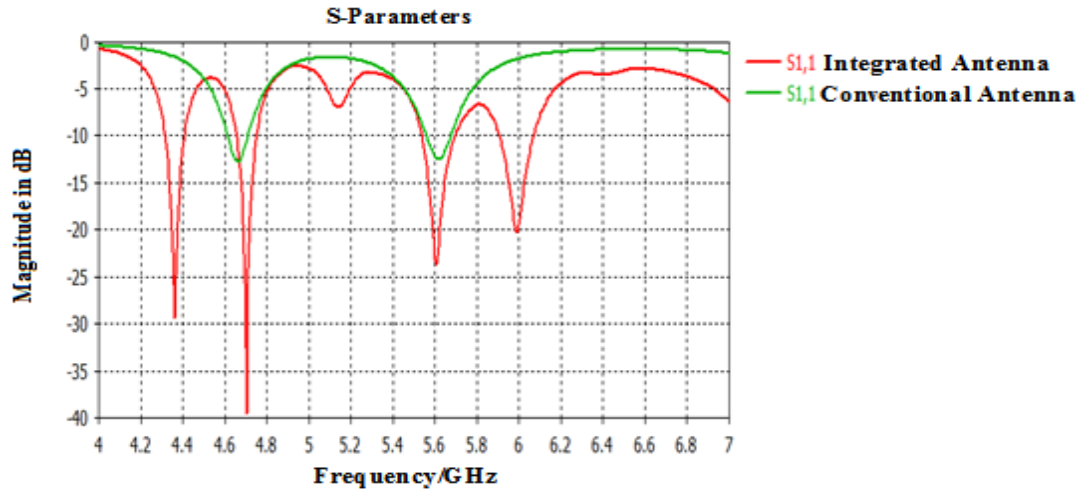
Fig.2. Comparison of Conventional and Multi-Band Antennas.

The effect of RRPs and CSRR metamaterial was positive, the simulation results show that the integrated antenna generated four bands with high return losses, So that gives the antenna a multi-band characteristics compared with dual-band conventional which has poor return loss. Also note that the frequency shift is very little, so that means the coupling between the complementary split rings is very high.

Table1. Dimensions and Parameters of Quad-Band Antenna.

feeder	coaxial feed
Material of Substrate	FR-4 (Lossy)
Material of Patch	Copper (pure)
Material of RRPs	Copper (pure)
Effective dielectric constant	4.3
L1	27 mm
W1	31.7 mm
L2	24.8 mm
W2	31.2 mm
distance between rings d1	9mm
d2	1mm
g	0.5mm
R	2.3mm
r	1.85mm
L3	25mm
W3	29mm

substrate thickness	1.4 mm and 0.2 mm
patch thickness	0.02 mm
RRPs thickness	0.017mm
ground thickness t	0.017 mm
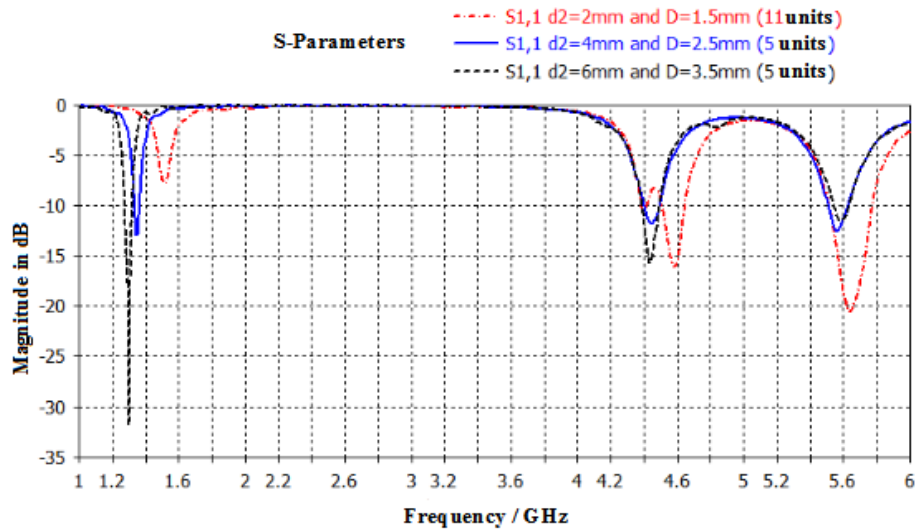
Fig.3. Return Loss at Variable Width d2, Variable Distance between Units D and Variable Number of Units.

Figure 3 Shows that by increasing the width and distance between RRPs, the return loss of WiMAX band will decrease and return loss of GPS band increase, that almost depend on the orthogonal patterns [9]. Increase the width and distance between RRPs effected on the coupling values between complementary split rings which led to shift the resonant frequencies. So, the purity of vertical polarization created by the excited metamaterial and RRPs will be affected. Although the possibility of use in the GPS applications, but that leads to several disadvantages including the weakening of WiMAX functions and other operating bands, also reduce the efficiency.

(a)

(b)
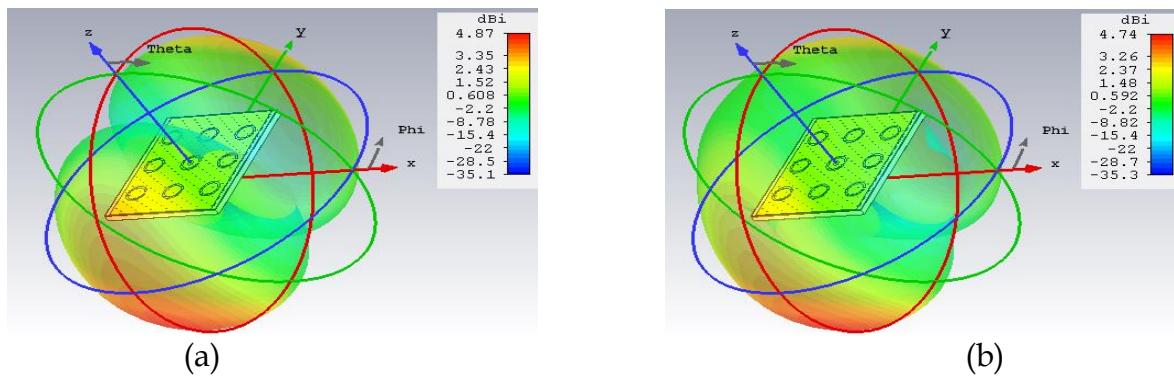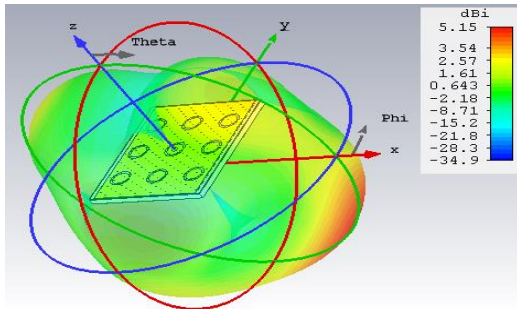
(c)
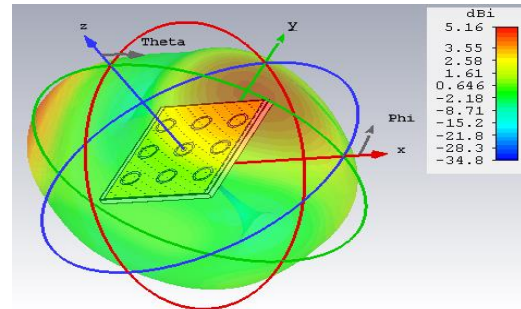
(d)
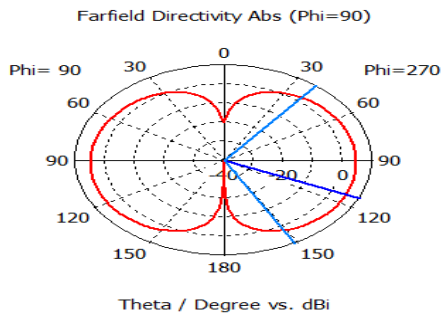
(e)
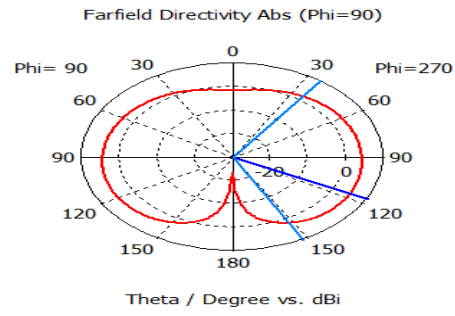
(f)
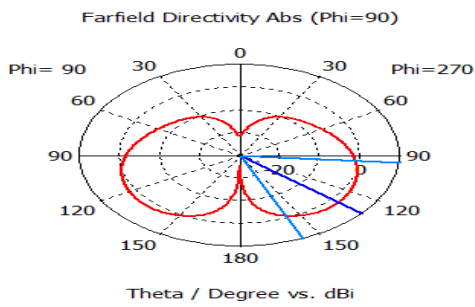
(g)
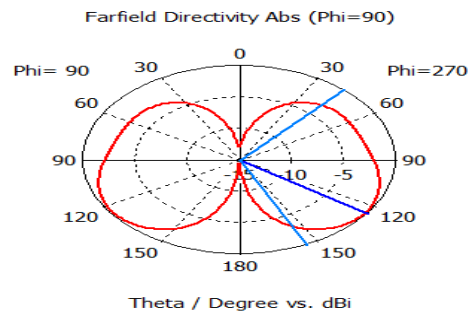
(h)

Fig.4. Radiation Pattern (RP) and Polar Plot (PP) of Multi-Band Antenna (a) RP at 4.36 GHz (b) RP at 4.7 GHz (c) RP at 5.6 GHz (d) RP at 5.99 GHz (e) PP at 4.36 GHz (f) PP at 4.7 GHz (g) PP at 5.6 GHz (h) PP at 5.99 GHz.

SIMULATION AND RESULTS

Figure 2 shows the return loss simulation of multi-band antenna compared with conventional. The use of RRPs and CSRs metamaterial give better results by increasing the number of bandwidth and enhancing the return loss. New antenna operates at (4.36 GHz, 4.7 GHz, 5.6 GHz and 5.99 GHz) with return loss (-29.4dB, -39.4dB, -23.6dB and   -20dB) respectively. The operating bands of antenna are 91

MHz at 4.36 GHz, 95 MHz at 4.7 GHz, 158 MHz at 5.6 GHz and 162 MHz at 5.99 GHz. Compared with conventional which operates at 4.66 GHz and 5.616 GHz with return loss -12.7dB, -12.5dB only and 95, 114 MHz bandwidth. 3D radiation pattern and polar plot for quad-band antenna were simulated. The simulating results appear in figure 4, where (a), (b), (c), (d) refer to radiation pattern and (e), (f), (g), (h) refer to polar plot. The directivity of antenna is 4.87 dBi, 4.74 dBi, 5.15 dBi and 5.16 dBi at 4.36 GHz, 4.7 GHz, 5.6 GHz and 5.99 GHz respectively, The beam main lobe direction is 6 degree with beam width 112.7 degree at 4.36 GHz, 3 degree with beam width 116.5 degree at 4.7 GHz, 10 degree with beam width 62 degree at 5.6 GHz and 5 degree with beam width 112.8 degree at 5.99 GHz.

STUDY THE BEHAVIOR OF CHDSs ON SEVERAL TYPE OF RIS

Observed through the simulation results that insertion of Circular Patch CP, RRPs or CRPs with CHDSs shows a dominant and consistent behavior of metamaterial on antenna. Analysis of this behavior would require many tests with several Reactive Impedance Surface RIS that operate at different frequencies. However, the use of CP with CHDSs was very important to understand that behaviour because changing the diameter of CP in each case was given a new frequency with the conventional antenna, On the other hand use of RRPs and CRPs also signifycant to test a different shapes with different dimensions.
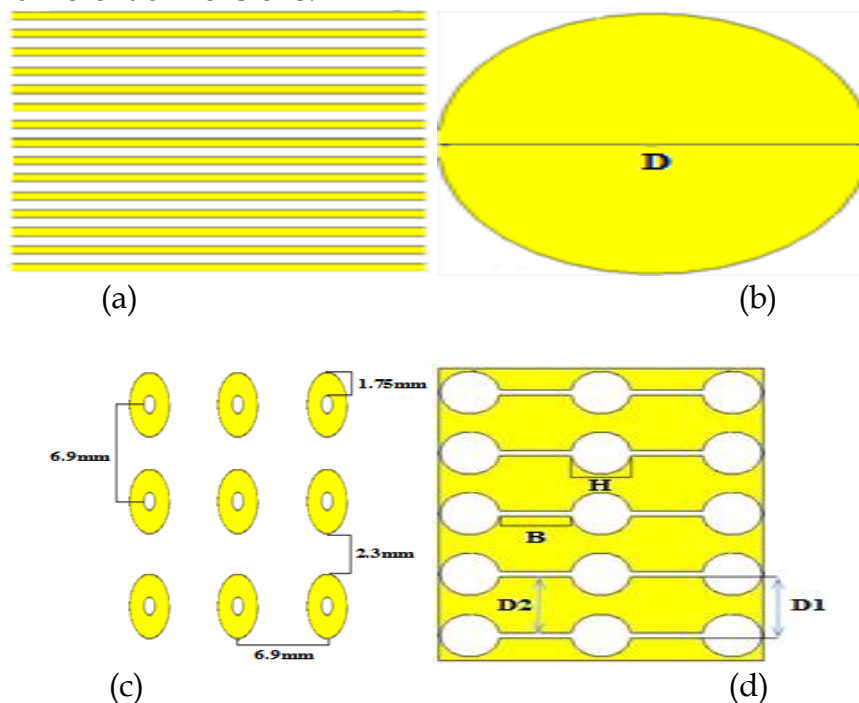
Fig.5. Shows the Shapes of RIS used with CHDS which are (a) Rectangular Ruler Patches, (b) Copper Circular Patch with Various Radius, (c) Circular Ring Patches, (d) Circular Head Dumbbel Structure with Dimensions of D1= 6.5mm, D2=6.0mm, B=5.43mm, H=4.57mm, Redius=2.3mm.

(a)

(b)

(c)

(d)

(e)
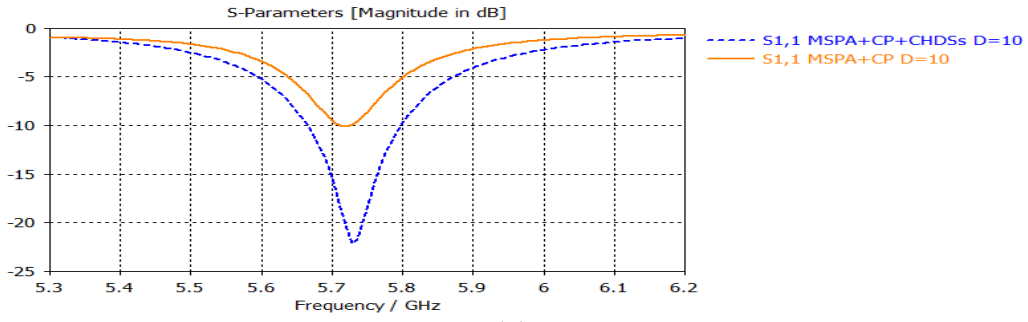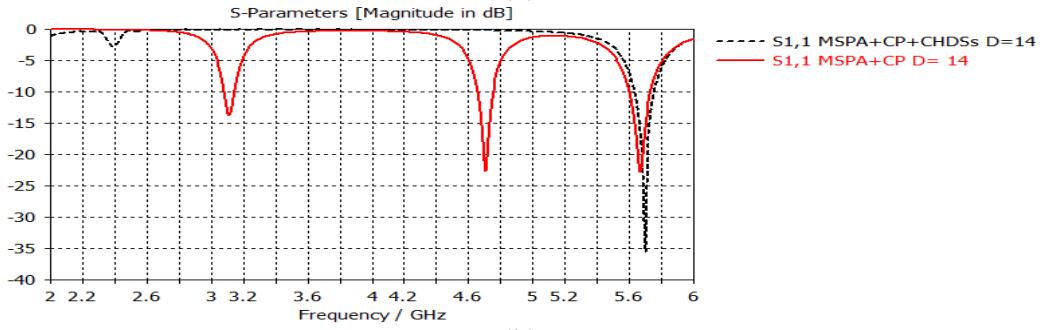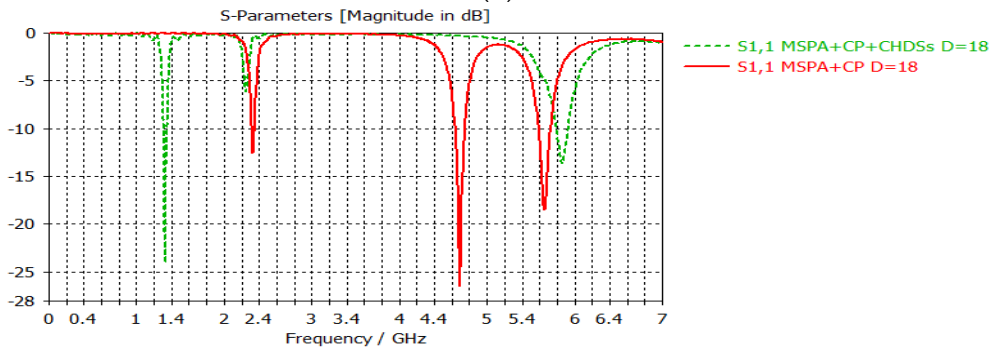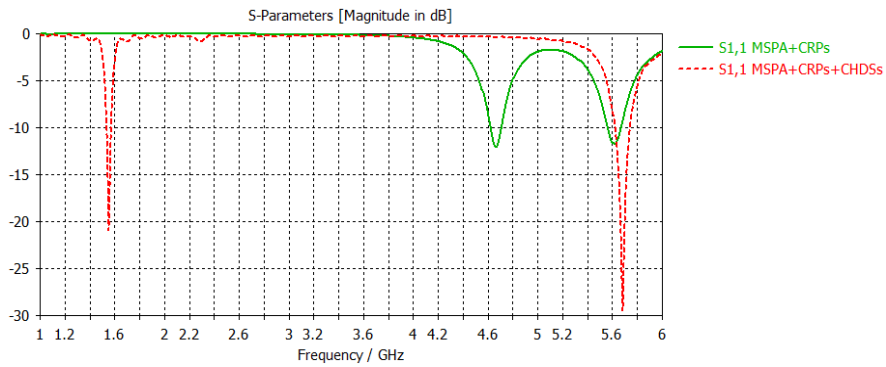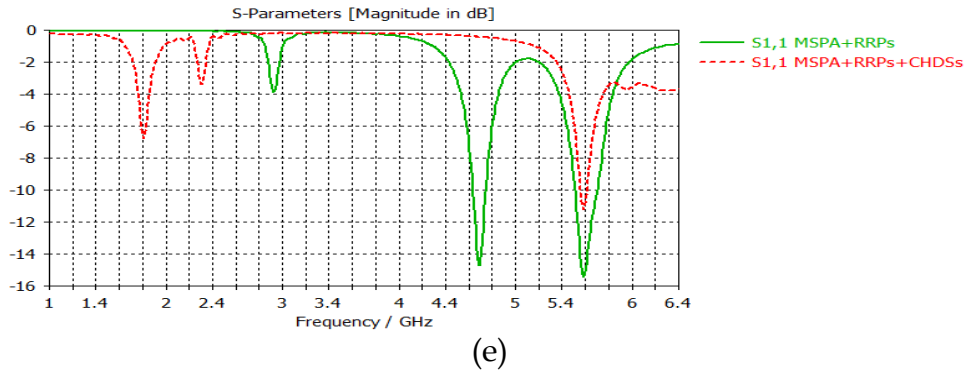
Fig.6. Shows Comparison between the use of RIS alone with the Conventional Antenna and the Effect of CHDS Behavior when added with. (a) CP at Diameter of 10mm, (b) CP at Diameter of 14mm, (c) CP at Diameter of 18mm, (d) CRPs, (e) RRPs.

Table2. Characteristics of RIS Effect on Conventional Antenna.

Parameter	RRPs antenna at 4.68 GHz	CRPs antenna at 4.66 GHz	CP antenna at 4.69 GHz D=16mm
Return loss dB	-14.7	-12	-33
Bandwidth MHz	109	89	106
Directivity dBi	5.21	5.16	5.31
Parameter	RRPs antenna at 5.58 GHz	CRPs antenna at 5.61 GHz	CP antenna at 5.65 GHz D=16mm
Return loss dB	-15.4	-11.7	-19.7
Bandwidth MHz	192	103	135
Directivity dBi	5.45	5.34	5.26
Parameter	RRPs antenna at 2.65 GHz	CRPs antenna at 2.65 GHz	CP antenna at 2.65 GHz D=16mm
Return loss dB	-	-	-25.9
Bandwidth MHz	-	-	57
Directivity dBi	-	-	2.23

From figure 6 and table 2, the behavior of the CHDS array was concluded. The study depends on the return loss of all RIS elements where observed that behavior of CHDS was consistent with all elements.

CHDS WITH CP

1. CP diameter=10mm

As previously mentioned that the return loss of conventional antenna is -12.2dB at 4.66 GHz and -12.1dB at 5.61 GHz. Return loss of CP at D=10mm without CHDS is less than conventional just -10.1dB at 5.7 GHz. Adding CHDS increased the return loss to -22dB, also enhanced the bandwidth from 12MHz to132MHz.

2. CP diameter =14mm

Return loss of CP at D=14mm without CHDS is higher than conventional and has three bands, -22.8dB at 5.66 GHz,   -22.6dB at 4.7 GHz and -13.8dB at 3.1GHz with good bandwidth of 132MHz, 95MHz and 62MHz respectively. Adding CHDS removed the band of 4.7 GHz and 3.1 GHz with raise in return loss of 5.6 GHz to -35.5dB and reducing the bandwidth.

3. CP diameter=18mm

Return loss of CP at D=18mm without CHDS has three bands, -18.46dB at 5.65 GHz, -26.5dB at 4.68 GHz and   -12.5dB at 2.3 GHz with good bandwidth of 135 MHz, 110 MHz and 32 MHz respectively. Adding CHDS removed the band of 4.68 GHz with decrease in return loss of 5.6 GHz to -13.6dB and shift the band of 2.3 GHz to 1.3 GHz with high return loss of -24dB and 37 MHz bandwidth.

CHDS WITH CRPs

Return loss of CRPs without CHDS is less than conventional of -12dB at 4.66 GHz and -11.7dB at 5.61 GHz with less bandwidth of 89MHz and 103MHz respectively. Adding CHDS improved the return loss and bandwidth to -28.2dB and 123MHz at 5.6 GHz and shifted the band of 4.66 GHz to 1.55 GHz with increase in return loss of -18.8 dB.

CHDS WITH RRPs

Return loss of RRPs without CHDS is -14.7dB at 4.68 GHz and -15.4dB at 5.58 GHz with bandwidth of 109MHz and 192MHz respectively. Adding CHDS reduced the return loss and bandwidth to -11.16dB and 52MHz at 5.58 GHz and removed the band of 4.68 GHz.

Conclude from that, CHDS metamaterial deals with RIS elements according to their effect on the conventional antenna as following, If the return loss of the RIS is less than -10, but has a negative impact on the conventional antenna by reducing its return loss, the CHDS will increase the return loss and bandwidth of WiMAX frequencies which between (5.25-5.85) GHz [12-13] and shifts 4, 3, 2 GHz frequencies band to the GPS band. If the return loss of the RIS is between (-10dB to -20dB) and has higher return loss than conventional, the CHDS will reduce the return loss and bandwidth of WiMAX frequencies that between (5.25-5.85) GHz and removes 4, 3, 2 GHz frequencies band. If the return loss of the RIS is less than -20 and higher than conventional, the CHDS will increase the return loss and decreases bandwidth of

WiMAX frequencies which between (5.25-5.85) GHz and removes 4, 3, 2 GHz frequencies band.

CONCLUSION

Two types of metamaterial were used, both have generated circular polarization which produced by orthogonal of excited radial patterns with 90 degree [9], CSRR has used with RRPs to generate quad-band antenna for several applications, CHDS has used with several RIS and showed the same behavior, thus It can be used in WiMAX and GPS applications to enhance the received signals. Changing CHDS dimensions make it lose its properties.

(a)

(b)

(c)

(d)

(e)

(f)
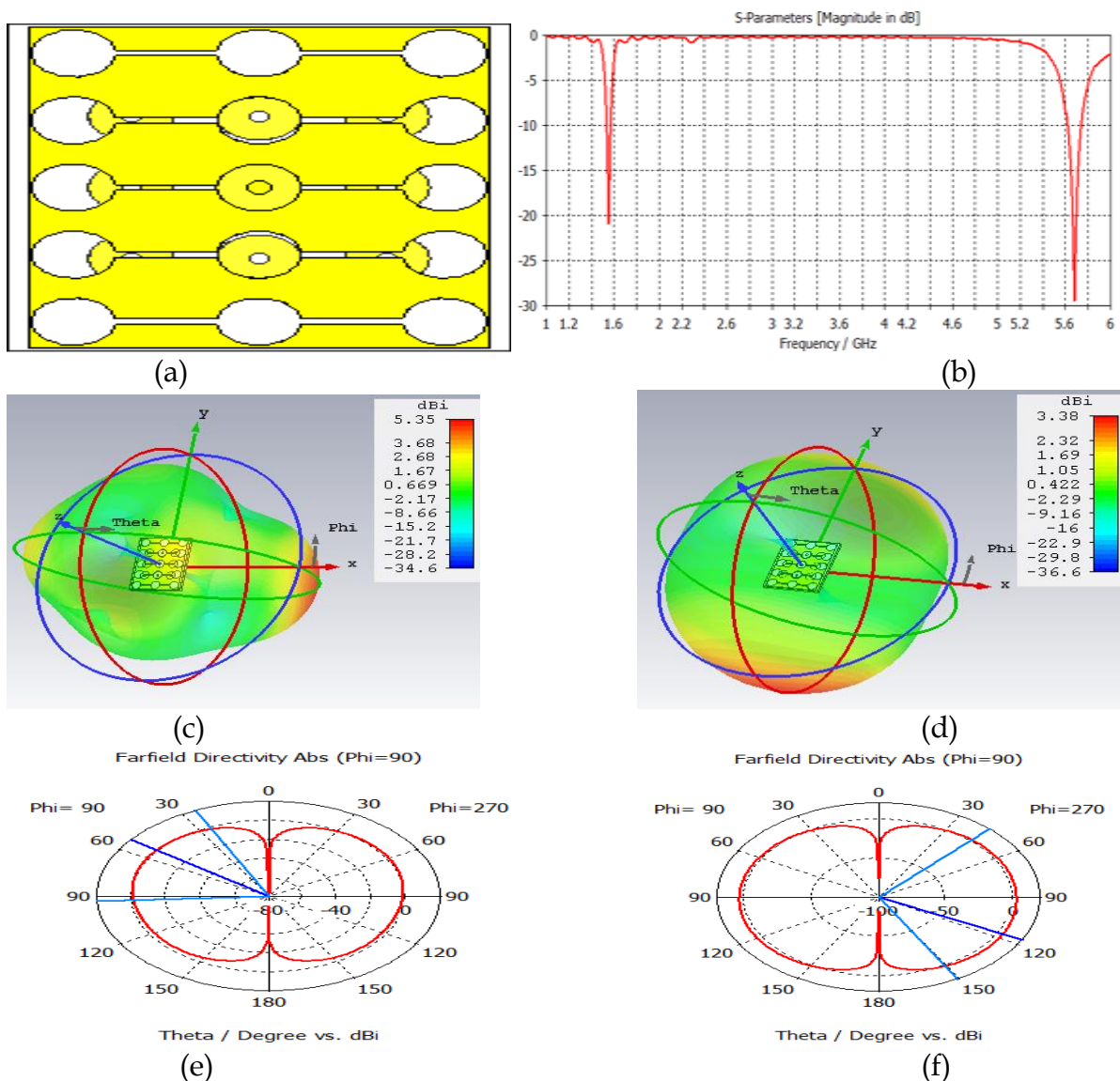
Fig.7. Return Loss, Radiation Pattern (RP) and Polar Plot (PP) of Dual-Band Antenna by using CHDS plus CRPs (a) Integrated Antenna, (b) Return Loss, (c) RP at 5.68 GHz, (d) RP at 1.55 GHz, (e) PP at 5.68 GHz, (f) PP at 1.55 GHz. 3D Radiation Pattern and Polar Plot for Complementary Antenna were simulated.

The simulating results appear in figure 4.12, where (a), (b) refer to Radiation Pattern and (c), (d) refer to Polar Plot. The Directivity of Antenna is 5.35 dBi and 3.38 dBi at 5.68 GHz and 1.55 GHz respectively. The Beam Main Lobe Direction is 7 degree with Beam Width 68 degree at 5.68 GHz and 3 degree with Beam Width 107.4 degree at 1.55 GHz.

REFERENCES

[1] BALANIS C. A., Antenna Theory: Analysis and Design, 2nd Edition, Wiley, New York, 1997.

[2] Howell, J., "Microstrip antennas," Antennas and Propag-ation, IEEE Transactions on, vol.23, no.1, pp. 90-93, Jan 1975.

[3] G. A. Deschamps, "Microstrip microwave antennas," prese-nted at the Third USAF Symp. on Antennas, 1953.

[4] Pozar, D.M., "Microstrip antennas," Proceedings of the IEEE , vol.80, no.1, pp.79-91, Jan 1992.

[5] C.A. Balanis, "Antenna Theory Antenna Analysis & Design , 2nd edition, John Wiley& Sons, Inc. 1993.

[6] MOSALLAEI H., K. Sarabandi, Antenna miniaturization and bandwidth enhancement using a reactive impedance sub-strate, IEEE Trans. Antennas Propag., vol.52, no.9, 2004, 2403 – 2414.

[7] DONG Y., TOYAO, H., ITOH, T., Design and character-ization of miniaturized patch antennas loaded with complemen-tary split-ring resonators, IEEE Trans. Antennas Propag., vol.60, no.2, 2012, 772 - 785.

[8] Huda A. Majid, Mohamad Kamal A. Rahim, and Thelaha Masri, "Left Handed Metamaterial Design for Microstrip Ant-enna Application", IEEE International RF and Microwave Con-ference Proceedings, December 2-4, 2008.

[9] BAENA J. D., et al., Equivalent-circuit models for split-ring resonators and complementary split-ring resonators coupled to the planer transmission lines," IEEE Trans. on Microwave The-ory and Techniques, vol. 53, no. 4, 2005, 1451 – 1461.

[10] D. Sarkar, K. V. Srivastava, and K. Saurav, "A compact microstrip fed triple band-notched ultra-wideband monopole antenna," IEEE Antennas Wireless Propag. Lett, vol. 13, pp. 396–399, 2014.

[11] K.Saurav, D. Sarkar, and K. V. Srivastava, "Dual-Polarized Dual-Band Patch Antenna Loaded With Modified Mushroom Unit Cell," IEEE Antennas Wireless Propag. Lett., vol. 13, pp. 1357–1360, 2014.

[12] C.A.Balanis, Antenna Theory: Analysis and Design, 2nd ed. New Delhi, India: Wiley, 2007.

[13] R.Garg, P.Bhartia, I.Bahl, and A.Ittipiboon, Microstrip Antenna Design Handbook. Boston, MA, USA: Artech House, 2001.

[14] Enge, P.; Misra, P., "Special Issue on Global Positioning System," Proceedings of the IEEE, vol.87, no.1, pp.3-15, Jan 1999.

[15] WANG J., YIN, Y.Z., XIE, J.-J., PAN, S.L., WANG, J.-H, LEI, X., A compact multiband monopole antenna for WLAN /WiMAX applications, Progress In Electromagnetics Research Letters, vol.23, 2011, 147-155.

AN EXPERIMENTAL STUDY ON THE DETERMINATION OF THERMAL CONDUCTIVITY, HEAT CAPACITY AND THERMAL DIFFUSIVITY OF A POROUS METAL FOAM

Ozkan KIREC
Mechanical Engineering Department, University of Gaziantep
ozkankirec@gantep.edu.tr

Melda Ozdinc CARPINLIOGLU *
Mechanical Engineering Department, University of Gaziantep
melda@gantep.edu.tr
* Corresponding Author

ABSTRACT : Porous metal foams are novel heat transfer surfaces with the potential use as heat sinks and heat exchangers. In the presented study, thermal characteristics of porous metal foams which are modeled as bulk micro-channel patterns in relevance to the material characteristics are the main topic of discussion given in this paper. An experimental investigation based upon a modeling approach through the measurements of local temperatures along the x-y-z axis of the porous copper foam samples was conducted. A variety of plate type copper foam samples with a size of 150 mm (L), 30 mm (W) and 3 mm, 4 mm, 5 mm (t) with 95 % porosity are tested and physical analysis is presented at heating surface temperatures of T_H = 50 ˚C for Θ = 10 min.. Effects of the cooling time is also given at T_H = 80 ˚C for Θ = 10 min. Time dependent thermal views of the samples are taken by usage of thermal imaging camera. Experimental results compared with copper foil reference items are presented to see the various effects of the porous medium on heat transfer. Scanning electron microscopy (SEM) device is used for analyzing the micro-structure of the samples. Local changing of the thermal conductivity, k heat capacity, C and thermal diffusivity, α are calculated as a function of different parameters.
The experimental results showed that, k, C and α values of the porous copper foams and copper foil reference items change between 250 W/m.K ≤ k ≤ 517 W/m.K and 40 W/m.K ≤ k ≤ 120 W/m.K, 250 J/K ≤ C ≤ 710 J/K and 255 J/K ≤ C ≤ 715 J/K, 5 mm²/s ≤ α ≤ 42 mm²/s and 0.1 mm²/s ≤ α ≤ 0.8 mm²/s depending on the T_H, t and Θ.

Key words: Copper Foam, Temperature, Porous Medium, Porosity, Thermal Conductivity, SEM

INTRODUCTION

The concept of porous media is used in many areas of applied science and engineering. Using porous media to extend the heat transfer area, improve effective thermal conductivity, mix fluid flow and thus enhance heat transfer is an enduring theme in the field of thermal fluid science. According to the internal connection of

neighbouring pore elements, porous media can be classified as the consolidated and the unconsolidated. For thermal purposes, the consolidated porous medium is more attractive as its thermal contact resistance is considerably lower. Especially with the development of co-sintering technique, the consolidated porous medium made of metal, particularly the metallic porous medium, gradually exhibits excellent thermal performance because of many unique advantages such as low relative density, high strength, high surface area per unit volume, high solid thermal conductivity, and good flow-mixing capability [1] (Xu et al., 2011b). It may be used in many practical applications for heat transfer enhancement, such as catalyst supports, filters, biomedical implants, heat shield devices for space vehicles, novel compact heat exchangers, and heat sinks, et al. [2-5] (Banhart, 2011; Xu et al., 2011a, 2011b, 2011c). In the last decade, open cell metal foams both stochastic and periodic have been largely studied through experimentation and analysis. New and innovative heat transfer techniques are needed for heat transfer enhancement and pressure drop research and development studies.

In this view, porous metal foams are good candidate for these purposes. There are many studies to analyse the material characteristics of metal foams. Calmidi [6] proposed the use of cubic unit cell model to approximate the metal foam structure and proposed a relationship of pore diameter (d_{pore}) as a function of porosity (ε) and pore density (PPI). Du Plessis et al. [7] presented a model for evaluating permeability (K) and inertia coefficient for metal foams which was derived by experimental results of foam samples of small pore size (45-100 PPI) and porosity of 0.973-0.978 with water and glycerol as fluid phase. Kurtbas et al. [8] conducted an experimental study for investigating the heat and exergy transfer characteristics of forced convection in a horizontal rectangular channel with inserted aluminum open cell metal foam under constant heat flux, using different pore densities (10, 20, 30 PPI). They found that the aluminum open cell metal foam has a considerable effect on the thermal performance when they compare their results with the empty channel. Ghosh [9] performed a systematic study to give an overview related to heat transfer in a metal foam and asked ''How good is open-cell metal foam as a heat transfer surface?''. In his study, the effect of area density as functions of pore size and strut diameter were discussed. He concluded that foams are a promising alternative for compact heat exchangers due to the ideal thermodynamic characteristics. Literature reviews show that there are very limited data and studies are available on thermal characteristics of porous copper foams. Performance of copper foams for heat transfer enhancement purposes should be studied.

As a result, analysis of micro / mini channels as porous structures are studied as a function of different parameters for future scopes of enhancing thermal performance of channels.

EXPERIMENTAL METHODOLOGY

Porous Medium: Porous media with high thermal conductivity have emerged as an effective method of heat transfer enhancement due to their large surface area to

volume ratio and to intense mixing of the flow. Porosity can be calculated depended of volume of both sample and solid [10] Kaviany :

$$\varepsilon = 1 - (V_{solid} / V_{sample})$$

(1)

Use of porous metal foams in heat transfer applications is novel. Consequently, numerous investigations have been carried out on this subject in the recent past. For the experimental studies, different shapes, sizes and thicknesses copper foams are used as a test sample listed in the Table 1.

Table 1. Properties of The Copper Foam Samples

Shape	Dimension (mm)	Porosity (%)	PPI	Density (g/cm3)
Plate	150*30* 3			
	150*30*4	95	40	0.45
	150*30*5			

Copper foams are produced with specified dimensions and properties by manufacturing company, Beijing Shunyuan Wangda Trade Co., in China. To perform and analyze the local temperature variations in porous medium, a heater unit is used as a heat source.

Copper foams are located on it with different thicknesses. Heater temperatures (T_H) are T_H = 50 ˚C which are used as case temperatures to analyze the thermal characteristics of the copper foams. Thermal image views of the copper foams are taken periodically for Θ = 10 min. by Testo 875-2i thermal image camera and temperature variations along the selected region or directions are taken as a case measurement.

The thermal camera provides thermal imaging with a high level of thermal sensitivity, outstanding image quality and allowing hot and cold spots to be quickly visible. Hence, the smallest temperature differences can be seen. To describe the effects of the micro-structure of the copper foams on heat transfer performance, scanning electron microscopy (SEM) device is used. The key parameters for this research: heater temperatures, geometry of the copper foam samples, porosity, pore size and time periods.

Heating And Cooling Experiments

Two different experiments are considered. These are called as heating and cooling experiments. In the heating experiments, test samples are located on to the heater unit with a specified T_H of 50 ˚C are shown in Figure 1 and are waited for Θ = 10 min.

Thermal camera views of the test samples are taken at the end of the time period from the upper surface of the samples and also from the contact surfaces by reversing the sample upper surface. These thermal views are used for analysing the thermal behaviour of the test samples. In the cooling experiments, test samples' contact surfaces, which exposed to a T_H = 50 ˚C through heating process for Θ = 10 min. time period, are located on reference plate of white paper at room temperature until the contact surface temperature comes to room temperature, T_R values. Thermal views of the contact surfaces are taken periodically for Θ = 0, 3, 6 and 10 min.
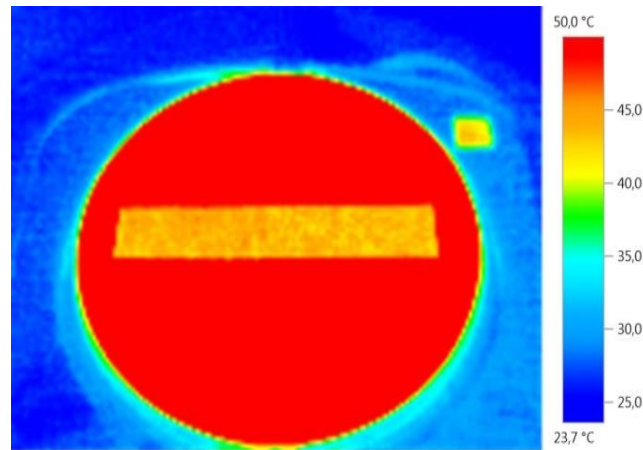
Figure 1. Location of The Samples on The Heater Unit

Temperature Measurements on The Tested Copper Foam Samples

Defining the thermal characteristics of the porous copper foam materials along the all surface points, use of the temperature measuring device with high sensitivity plays important and critic role for certain and precise experimental results.

Settings of the thermal imaging camera with respect to material properties before taking the thermal views of the copper foams are also key points. Especially setting of the heater temperatures, emissivity value of the material, quality of the thermal views and correct position of the measuring device are also critical points for taking the correct results.

As a case study, plate type copper foam samples with different thicknesses, t which t = 3 mm, t = 4 mm and t = 5 mm shown in the Figure 2, are arranged on heater surface at T_H = 50˚C for 10 min. and temperature variations on the upper and contact surfaces of the copper foams are measured by thermal camera instantly. Thermal camera focused precisely on copper foam material at same distance and position. Image clarity set by manually. After taking the thermal image views of the material, all image views are transferred to the computer for thermal analysis. Thermal images are analyzed with testo software program shown in the Figure 3. Thermal analysis results are given in the Figure 4.
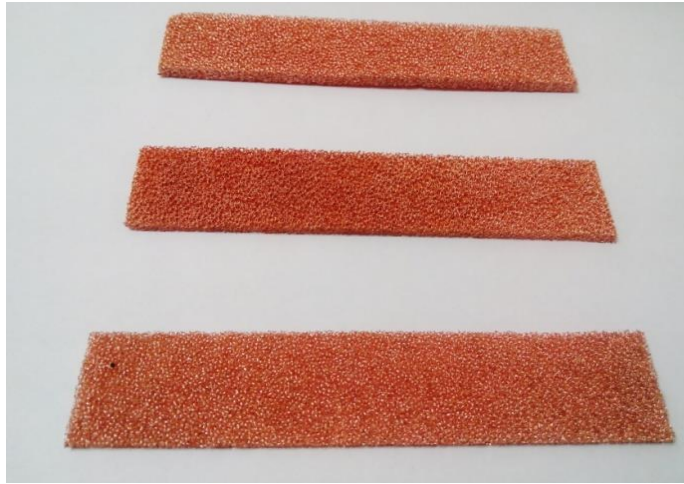
Figure 2. Plate Type Copper Foam Test Samples
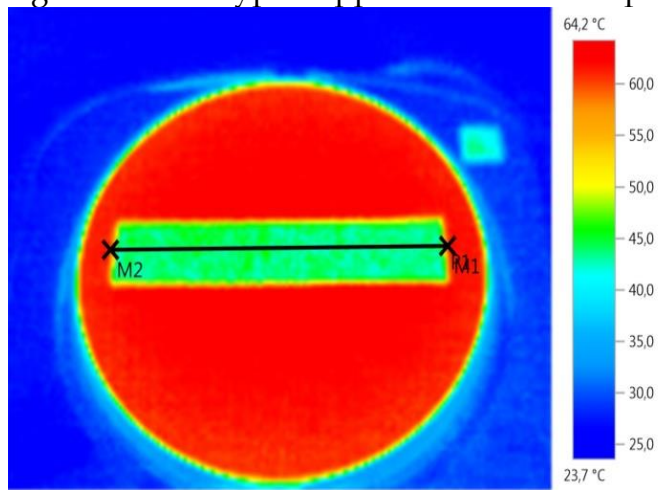
Figure 3. Thermal View and Temperature Distribution of The Copper Foam Sample
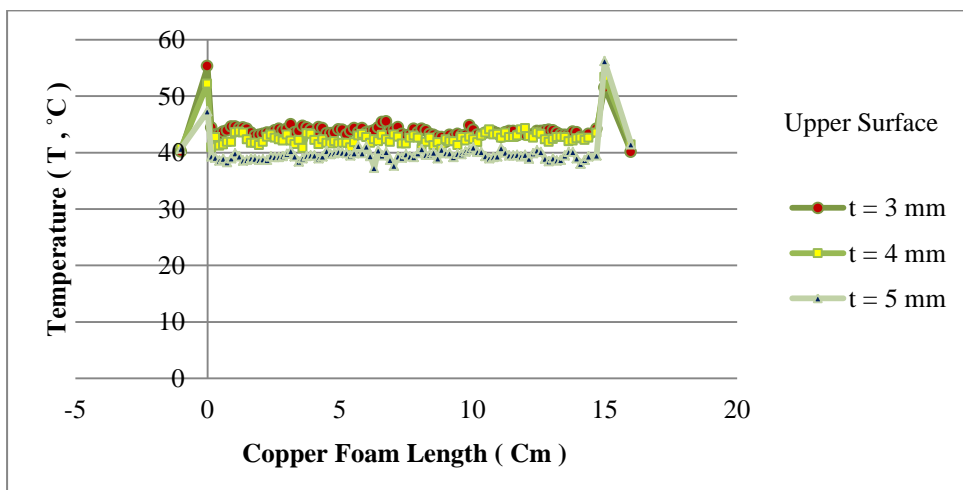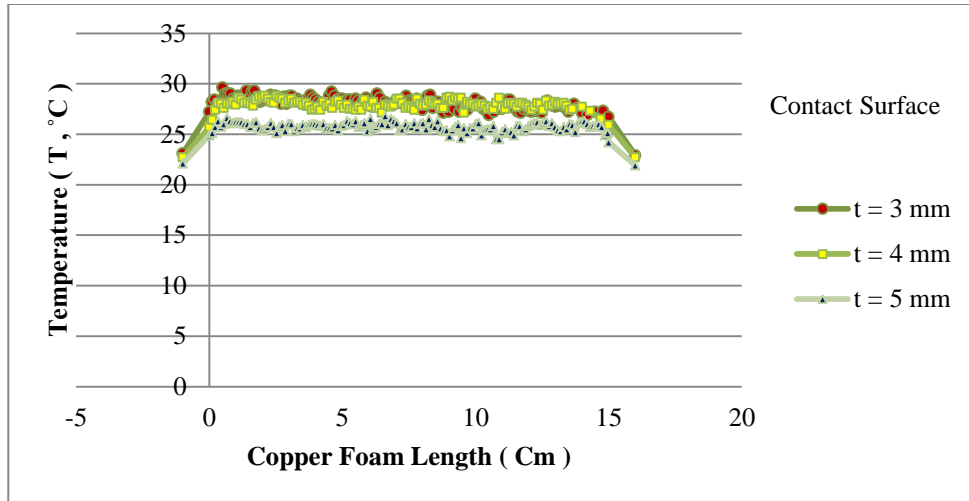
Figure 4. Copper Foam Upper and Contact Surface Temperature Profiles

It is seen from the Figure 4 that, upper surface temperature values of t = 5 mm Cu foam sample are lowest compared with other sample thicknesses. Mean temperature values for t = 3 mm Cu foam sample, 42.5 °C, for t = 4 mm Cu foam sample, 41.5 °C and for t = 5 mm Cu foam sample, 39 °C. Similarly, contact surface temperature values of t = 5 mm Cu foam sample are lowest compared with other sample thicknesses. Mean temperature values for t = 3 mm Cu foam sample, 28 °C, for t = 4 mm Cu foam sample, 27.9 °C and for t = 5 mm Cu foam sample, 25.7 °C

SEM Analysis of The Copper Foam Sample

Micro-structure of the copper foam from a heat transfer point of view, a scanning electron microscope (SEM) device is used. Micro-structure of the copper foam specimens observed at a wide range. Figure 5 and Figure 6 show the micro-structure of the copper foam material.
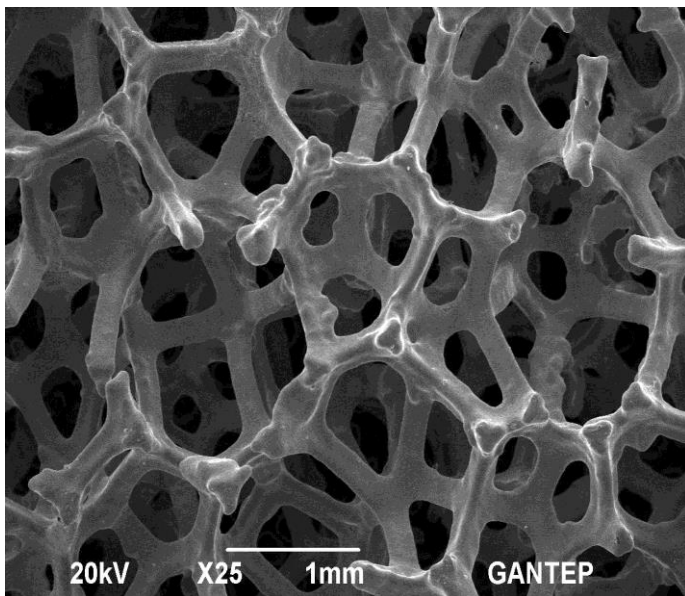
Figure 5. SEM Image of The Copper Foam
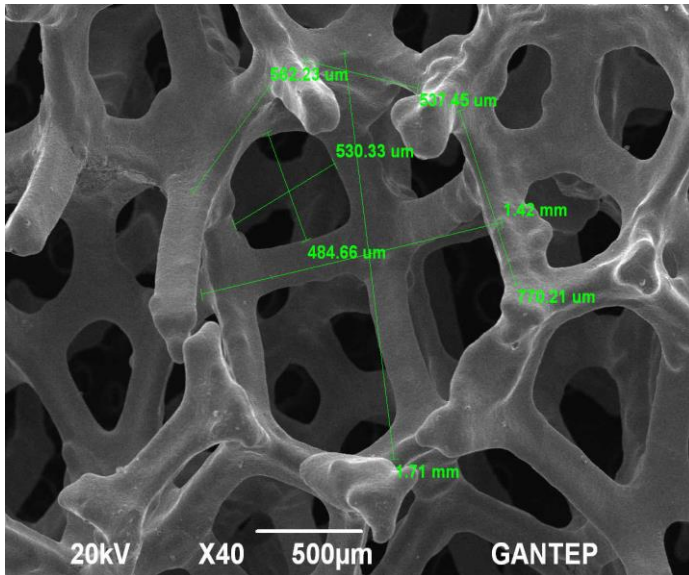
Figure 6. Unit Cell Image with Measured Dimensions

Scope investigations of the research listed as:

Effects of the micro-structure on heat transfer performance of the copper foam.

Observe and define the effects of pore shape, size, and directions on heat transfer

Defining the thermal behaviour of the material by means of thermal conductivity and heat capacity as well as thermal diffusivity.

THERMAL CHARACTERIZATION OF THE POROUS COPPER FOAM SAMPLES

Many different research groups have studied the heat transfer characteristics of these porous medium, experimentally and analytically. It is a widely held view that metal foams are still incompletely characterized because of their specific structure. The information repository is improving with time whereas the widespread use of the high porosity media in modern technological devices makes the need for fully characterizing them more urgent. Developments on this issue would certainly help engineering researchers, especially in terms of heat transfer [11,12]. In this study, thermal characteristics of the copper foam samples observed by means of thermal conductivity, heat capacity and thermal diffusivity. Changes of the k, C and α values of the Cu foam samples and Cu foil reference items at $T_H = 50°C$ for $\Theta = 10$ min. are given in the Figures 7, 8 and 9.
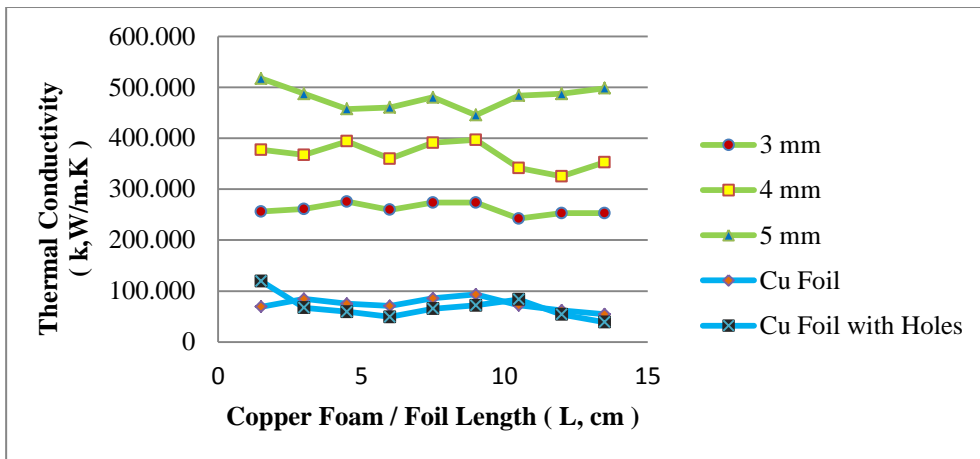
Figure 7. Variations of The Thermal Conductivity of The Cu Foams / Foil Samples at T_H = 50 ˚C

Results from the Figure 7 give some informations; k values of the Cu foam and Cu foil samples change from point to point and depend on the Ө which can be seen along the surface. It is clear from the figures that if thicknesses of the Cu foam increase then k increases. This situation shows the effects of the porous medium on k. It is seen from the Figure 7 that, t = 5 mm Cu foam sample has higher k than the other thicknesses of the samples. Values of the k change between the (250 W/m.K – 275 W/m.K) for 3 mm, (320 W/m.K – 400 W/m.K) for 4 mm and (440 W/m.K – 517 W/m.K) for 5 mm Cu foam sample. On the other hand, Cu foil reference samples k values change between the (50 W/m.K – 93 W/m.K) for Cu foil and (40 W/m.K – 120 W/m.K) for the Cu foil with holes.
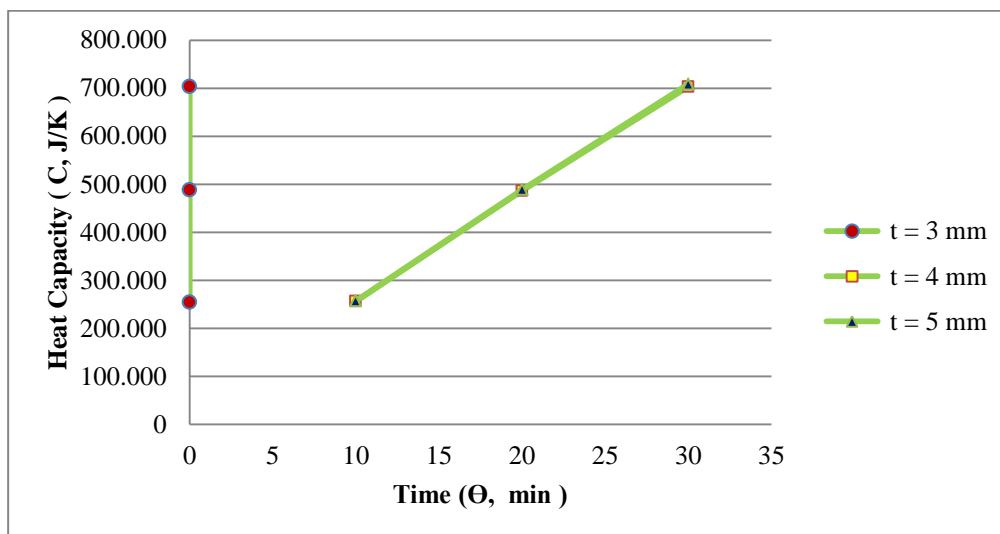
Figure 8. Time Dependent Heat Capacity Variations of The Cu Foams at T_H = 50 ˚C

As can be seen from the Figure 8 effects of the t are low for the specified T_H. Time dependent variations of C values of t = 3 mm Cu foam sample change between 254

J/K ≤ C ≤ 704 J/K, 250 J/K ≤ C ≤ 703 J/K for t = 4 mm Cu foam and 256 J/K ≤ C ≤ 709 J/K for t = 5 mm Cu foam.

Heat capacity values of the porous copper foam samples change between 250 J/K ≤ C ≤ 710 J/K and 255 J/K ≤ C ≤ 715 J/K for copper foil reference item samples depending on the different parameters of T_H, t and Ө. Results show that there is a little difference between the test samples.
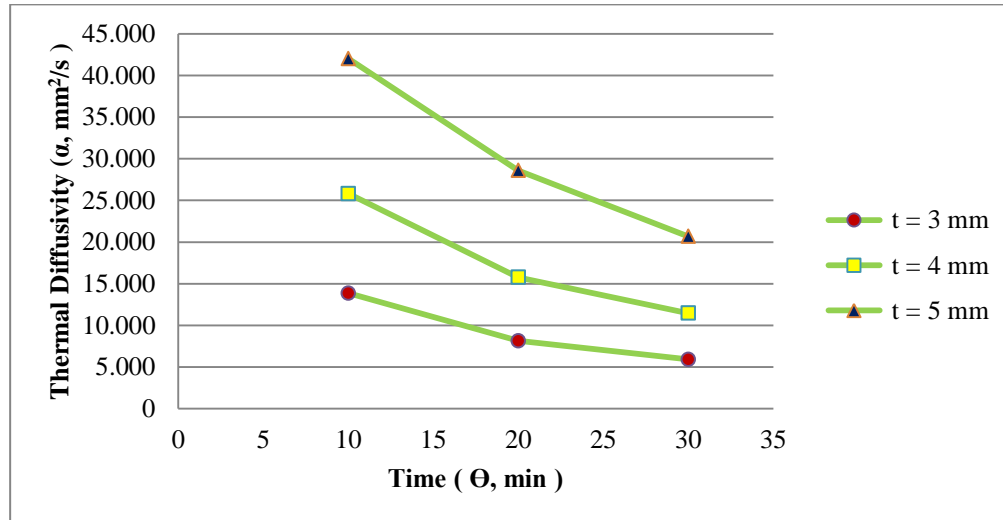
Figure 9. Time Dependent Thermal Diffusivity Variations of The Cu Foams at T_H = 50 ˚C

Analysis results from the Figure 9 show that, α values of the samples decrease depending on the Ө. α values of the 5 mm thickness Cu foam sample are higher than the other samples. α values of the samples change between the 5 mm²/s ≤ α ≤ 14 mm²/s for t = 3 mm, 11 mm²/s ≤ α ≤ 26 mm²/s for t = 4 mm and 20 mm²/s ≤ α ≤ 42 mm²/s for t = 5 mm at T_H = 50 ˚C.

As a result, thermal diffusivity of the porous copper foam samples change between 5 mm²/s ≤ α ≤ 42 mm²/s and 0.1 mm²/s ≤ α ≤ 0.8 mm²/s for copper foil reference item samples depending on the different parameters of T_H, t and Ө. These results show that speed of heat propagation inside the porous copper foam samples is much higher than the copper foil reference item samples.

Effects of The Cooling Time

In order to define the cooling performance of the Cu foam samples, analysis of effects of the cooling times on thermal profiles of the tested Cu foam samples are presented. Test samples' contact surfaces, which exposed to T_H = 80 ˚C through heating process for Ө = 10 min, are located on reference plate of white paper as a cooling medium until the contact surface temperature comes to T_R values. Thermal views of the contact surfaces are taken periodically for Ө = 0, 3, 6 and 10 minutes for t = 3 mm Cu foam sample and thermal profiles are shown and compared in Figure 10.
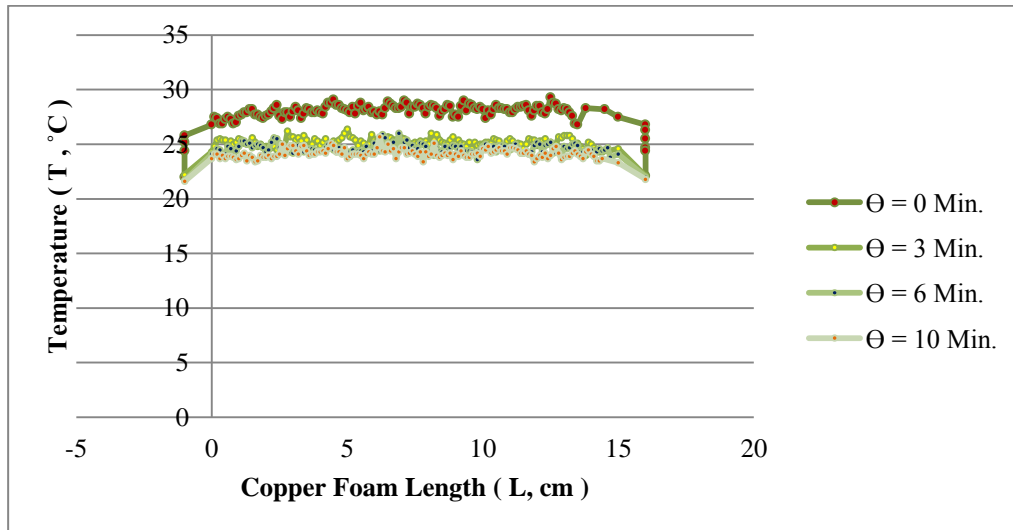
Figure 10. Thermal Profiles of 3 mm Thickness Cu Foam Sample at T_H = 80 ˚C as a Function of Θ.

It is obvious from the Figure 10 that, thermal profiles of the samples show high temperature values at Θ = 0 min. After the 0.min, thermal profiles show near temperature values depending on the increasing Θ. $T_{m, contact}$ values for Θ = 0, 3, 6 and 10 min. are 27.8 ˚C, 25.1 ˚C, 24.5 ˚C and 24.1 ˚C for t = 3 mm Cu foam sample. Figure 11 through Figure 14 shows the thermal images of the contact surface of the sample as a case for Θ = 0, 3, 6 and 10 min.
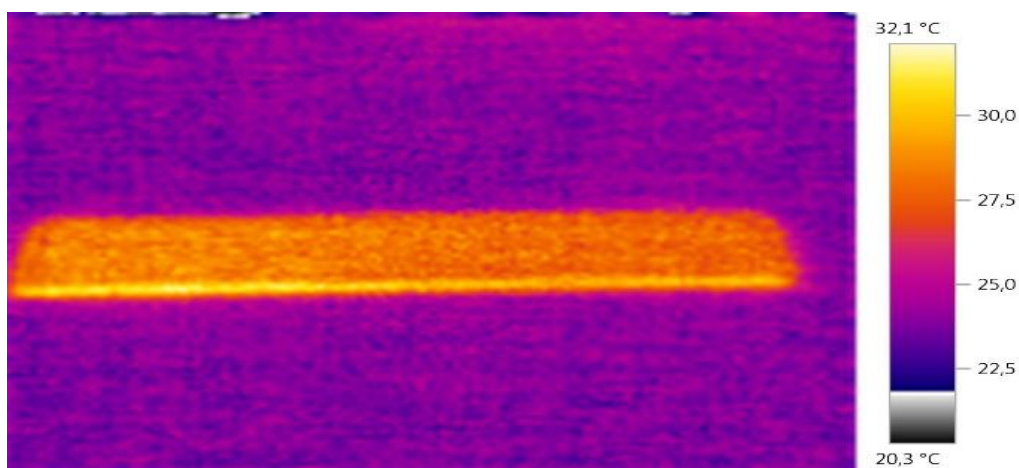
Figure 11. Thermal Image of The Test Sample For Θ = 0 min.
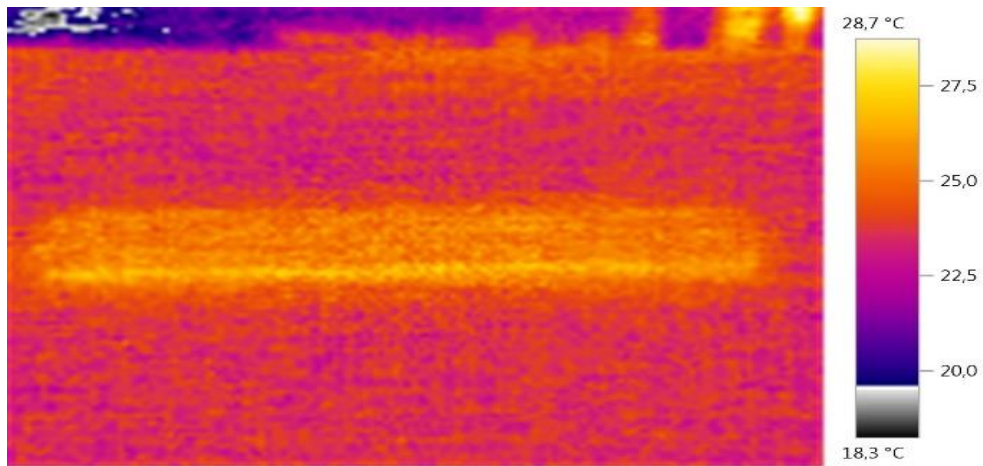
Figure 12. Thermal Image of The Test Sample For Ө = 3 min.
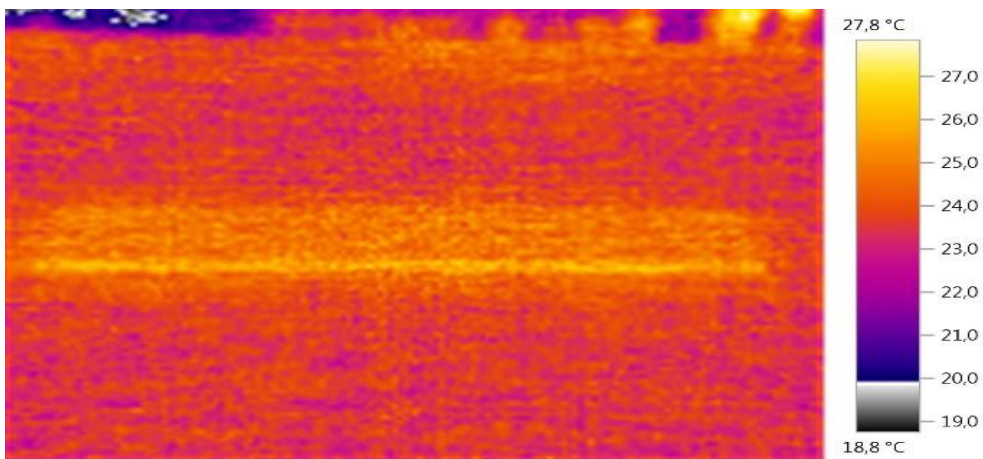
Figure 13. Thermal Image of The Test Sample For Ө = 6 min.
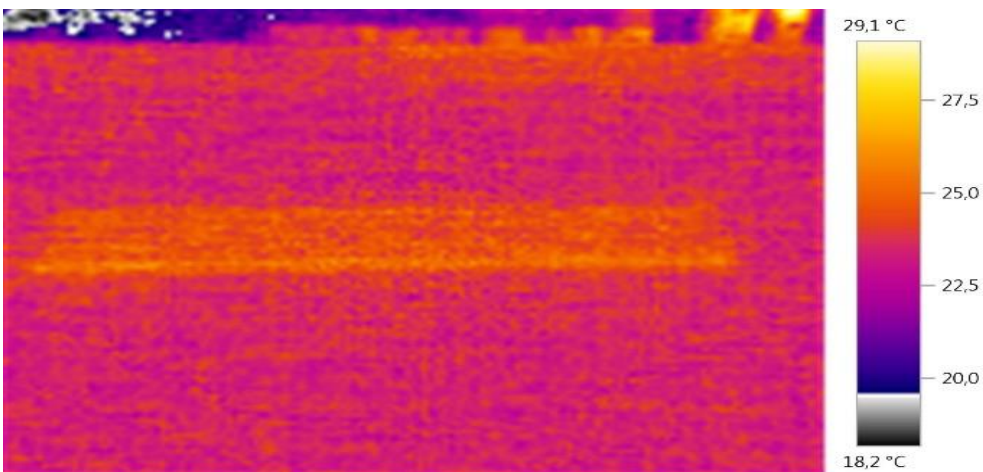
Figure 14. Thermal Image of The Test Sample For Ө = 10 min.

Thermal image views showed the time dependent heat transfer from the all surface of the sample. Analysis results gave information about the heat capacity properties of the sample. From the views and analysis, samples' contact surface temperature came to the surrounding temperature values in a short time.

CONCLUSION

Heat transfer characteristics of porous metal foams are experimentally and theoretically investigated. Copper metal foams are selected for conducted studies. All thermal image analyses of the samples as a function of different parameters are presented in detail. In order to define the thermal characteristics of the copper foam sample, thermal conductivity, heat capacity and thermal diffusivity analyses are given for different cases. Experimental results show the effects of the porous medium on heat transfer.

The results revealed that, micro-structure of the porous medium can have a significant effect on heat transfer. Especially, particular attentions are given to define the thermal characteristics of the material for further heat transfer investigations in many engineering fields.

RECOMMENDATIONS

Some suggestions are summarized and listed for future investigations ;
Optimising the design and production of porous metal foam structures for enhanging the heat transfer in micro channel.
Investigating the effects of the micro / nano porous metal foams on heat transfer.
Defining the relationship between geometrical properties and optimal heat transfer.
Developing the new models to deal with the fluid and thermodynamic challenges for complex porous structures.
Defining the thermal and material characteristics of the porous mediums for different cases and applications.
Developing the innovative porous metal foams for maximazing the heat transfer, especially for solving the cooling problems in many engineering fields.

REFERENCES

[1] Xu, H.J.; Qu, Z.G. & Tao, W.Q. (2011b). Thermal Transport Analysis in Parallel-plate Channel Filled with Open-celled Metallic Foams. International Communications in Heat and Mass Transfer, Vol.38, No.7, (August 2011), pp. 868-873, ISSN 0735-1933

[2] Banhart, J. (2001). Manufacture, characterisation and application of cellular metals and metal foams, Progress in Materials Science, Vol.46, No.6, (2001), pp. 559-632, ISSN 0079- 6425

[3] Xu, H.J.; Qu, Z.G. & Tao, W.Q. (2011a). Analytical Solution of Forced Convective Heat Transfer in Tubes Partially Filled with Metallic Foam Using the Two-equation Model. International Journal of Heat and Mass Transfer, Vol. 54, No.17-18, (May 2011), pp. 3846–3855, ISSN 0017-9310

[4] Xu, H.J.; Qu, Z.G. & Tao, W.Q. (2011b). Thermal Transport Analysis in Parallel-plate Channel Filled with Open-celled Metallic Foams. International Communications in Heat and Mass Transfer, Vol.38, No.7, (August 2011), pp. 868-873, ISSN 0735-1933

[5] Xu, H.J.; Qu, Z.G.; Lu, T.J.; He, Y.L. & Tao, W.Q. (2011c). Thermal Modeling of Forced Convection in a Parallel Plate Channel Partially Filled with Metallic Foams. Journal of Heat Transfer, Vol.133, No.9, (September 2011), pp. 092603.1-092603.9, ISSN 0022- 1481

[6] V.V. Calmidi, Transport Phenomena in High Porosity Metal Foams (Ph.D. Thesis), University of Colorado, Boulder, CO, 1998.

[7] P. Du Plessis, A. Montillet, J. Comiti, J. Legrand, Pressure drop prediction for flow through high porosity metallic foams, Chem. Eng. Sci. 49 (1994) 3545e 3553.

[8] I. Kurtbas, N. Celik, I. Dinçer, Exergy transfer in a porous rectangular channel, Energy 35 (2010) 451.

[9] I. Ghosh, How good is open-cell metal foam as heat transfer surface, Trans. ASME: J. Heat Transfer 131 (2009) 101004-1–101004-8.

[10] M. Kaviany, Principles of Heat Transfer in Porous Media, 2nd Edition, Springer, New York, 1995.
[11] N. Dukhan, K.C. Chen, Heat transfer measurements in metal foam subjected to constant heat flux, Exp. Therm Fluid Sci. 32 (2007) 624–631.

[12] N. Dukhan, P.D. Quiñones-Ramos, E. Cruz-Ruiz, M. Vélez-Reyes, E.P. Scott, One dimensional heat transfer analysis in open-cell 10-ppi metal foam, Int. J. Heat Mass Transfer 48 (2005) 5112–5120.

EFFECT OF STIFFENERS ON STRUCTURAL BEHAVIOR OF STEEL LIQUIDS TANK

Mahmood Hunar DHEYAALDIN
Research scholar, Department Civil Engineering
Mahmood.honer@gmail.com

Mustafa ÖZAKÇA
Professor, Department Civil Engineering
ozakca@gantep.edu.tr

Abubaker Sami DHEYAB
Research scholar, Department Civil Engineering
bakersami.bd@gmail.com

ABSTRACT: The finite element (FE) method is used to conduct an analysis of liquid storage tanks This research has focused on the behaviors, under static condition, free vibration and buckling of steel liquid tanks which are designed according to API 650 standards. The mechanical characteristics of the materials and the real geometrical and load measures have been considered in the numerical model. These storage tanks are connecting with American standard steel shape profiles. The equivalent stress (Von-Mises) distribution, deformation in the circular wall of the liquid tank, buckling load and fundamental frequency are computed using finite element method in order to investigate the effect of type of the stiffener, number of course and location of stiffener on the structural behavior of liquid tanks. The uses of the stiffener decrease the stress of wall tank and improve the other structural behaviors.

Key words: Finite element method, Stiffener, Storage tank, API-650 standard

INTRODUCTION

The design and maintenance of atmospheric and low-pressure vessels for liquid storage is becoming ever more vital as water and crude oil storage capacity utilization rises and water and oil storage capacity demands grow globally. On the other hand, failure of liquid storage tanks may lead to disaster due to the water crisis, fire, health and environmental hazard owing to the spread of chemicals or/and liquid fuel. Cylindrical tanks have been used in almost all sectors of industry, mainly as the tanks for storage of water or other liquids. Ground tanks, which are also known as reservoirs, can take different shapes (e.g. rectangular, cylindrical, and cylindrical with conical base). From the structural point of view, cylindrical tanks are very suitable as the external walls in the horizontal direction have been loaded only by tension or pressure, while in other types of tanks, the load is combined. Cylindrical tanks are appropriate also with respect to the low consumption of material needed for their construction. Presently more than 70 % of all tanks are of the circular ground plan. In a cylindrical liquid storage tank, it is

further classified, including the open top tank, fixed roof tank, external floating roof and internal floating roof tank. The type of storage tank used for the specified product is principally determined by safety and environmental requirements. Operation cost and cost-effectiveness are the main factors in selecting the type of storage tank (Chauhan, 2012).

There are two approaches for modeling liquid storage tanks by using analytical and numerical modeling techniques. The analytical modeling technique has been defined as a simplified model that had been developed by different researchers (Elkholy et al 2014) However, the analytical models including the fluid-structure interaction system and/or the soil structures integration system are very complex to solve. The most powerful numerical method is finite element (FE) method. In a method, the main objective is to create a mathematical representation of the engineering system that reflects its actual geometry and behavior (Housner et al 1963). The FE structural analysis program, ANSYS (Canonsburg, 2013b) was used in this study to produce the FE modeling needed for the tank analysis. Building FE models in ANSYS requires familiarity with the ANSYS operating manual and element library. Each element in ANSYS has specific properties and behaviors to be defined according to the structure in the problem (Elkholy et al, 2014) (Canonsburg, 2013a).

Because of the complexity added by the grid of rafters and rings, researchers and designers working on advanced analysis models to simulate the effect of such as fluid-structure interaction, soil structure interaction, buckling behavior, seismic load, wind load etc. (Burgos et al, 2015) Meanwhile, some of the researchers attempt to simplify the structural analysis by eliminating the three-dimensional grid and substituting it by a modification in the thickness of the roof. Such "equivalent" roof is a self-supported shell with a modified thickness, but also the weight needs to be adjusted in order to avoid having an excessively heavy roof which would buckle under self-weight. This approach may be found in many research papers (Fakhım et al 2009). Even simpler models have been considered in the literature, in which the roof is completely eliminated and its influence is represented by simply supported boundary conditions at the top of the cylindrical shell (Cao et al, 2010) Such simplifications are not motivated by computer time constraints but are frequently made to simplify modeling and data entry.

There are many numbers of options available for liquid tanks. Back in 1961, the American Petroleum Institute published the API Standard (API, 2013) which covers material, design, fabrication, erection, and inspection of petroleum tanks. The standard is designed to provide flexibility for the owner: As long as bulk oil storage tanks meet these minimum requirements, they can be of any size. Safety is a priority, but beyond that, a tank buyer has a lot of options.

The main objective of the present work is to investigate number of course, the number, location and type of stiffener on structural performance of liquids tanks. The cylindrical tanks are initially design based on API 650 code (API, 2013) In this preliminary design, wall thicknesses, number of courses and stiffener are evaluated. The FE structural analysis program, ANSYS (Canonsburg, 2013b) was used in this study to investigated the structural behavior of preliminary designed liquid shells in details. The critical buckling load, fundamental frequency, deformations and stress distribution in cylindrical liquid tank are computed.

Liquid Storage Tank Design

A tank design must first be completed using static analysis before evaluating and designing a tank for seismic loads and buckling. Many different tank configurations were chosen in order to encompass a wide range of results. These configurations were characterized by their ratio of height to the radius, commonly referred to as the aspect ratio. Low and high aspect ratios correspond to broad and slender tanks, respectively. Broad and slender tanks behave in different manners and, therefore, should be expected to have different limiting design criteria. For example, a tank with a large radius contains more liquid per foot of elevation than small radius tank, and therefore, would be expected to produce higher total inertial forces on the shell wall compared to a tank with identical height and smaller radius. In this sense, impulsive mass contributions increase with an increase in tank radius while maintaining a constant depth of liquid. Broad tanks, in general, generate larger free surface waves and therefore have higher convective mass proportions compared to tall, slender tanks. For high aspect, ratios stability can control the design, where overturning and uplift of unanchored tanks are of great concern, while material limits are still critical (Spritzer et al, 2017).

Tank design codes reflect the culmination of decades of work by many dedicated individuals. Using these standards helps to ensure that tanks will be able to stand the rigors of the elements and conditions to which they are subjected. They ultimately lie in the pages of the following codes and standards (Mayeux et al, 2016):

• American Petroleum Institute (API) 650 (API, 2013)
• BS EN 14015:2004 (British Standards Institution (BSI), 2004)
• API 620 (American Petroleum Institute, 2002)

Liquid storage tank design based on API 650

Tank thickness: The API 650 code can be used for designs of welded liquid storage steel tanks where the internal pressure is less than or equal to 2.5 psi. The calculation of the thickness of the liquid cylindrical storage tank is explained in Section 3.6 of API 650 (API, 2013) In this section, there are two methods for consideration:

• Calculation of Thickness by the 1-Foot Method
• Calculation of Thickness by the Variable Point Method.

The 1-foot method computes the required plate thickness at a distance of one foot above the bottom of each shell course and is applicable to tanks 200ft (61 m) and less in diameter. The basic equation in SI customary units looks something like this:

$$\text{thickness required} = \frac{4.9D(H - 0.3)G}{(S_d)(E)} + CA$$

The variable point method is an alternative to the 1-foot method and can be used for tanks in excess of 200ft (61 m) in diameter. The variable point equation in SI units is as follow

$$\text{Thickness required} = \left(1.06 - \frac{0.0696D}{H}\sqrt{\frac{H \times G}{S}}\right)\left(\frac{4.9H \times D \times G}{S}\right) + CA$$

Where: H is the design fluid height in m. D is the nominal tank diameter in m. G is the specific gravity of the contents. S is the tank wall material allowable tensile stress for the operating or test condition. CA is the corrosion allowance, if any API 650 storage tanks are often designed to work at temperatures of up to 500ºF (260ºC). For these higher temperature designs, the allowable stress of the material decreases. As a result, the required wall thickness increases in a linear fashion when using the 1-foot method and in a slightly non-linear fashion when using the variable point method. In addition to causing hoop stress and longitudinal stress in the tank wall, the slight internal pressure causes a tensile force (pressure × area) to be produced. This force pulls upward on the tank wall. This positive upward force is countered by the weight of the tank and roof (if not column-supported). If the net force is upward in any case or condition, the tank must be held down by anchor bolts. The basic internal pressure case is just one example. There are several other uplift formulas in Tables 5.21a (metric) and 5.21b (imperial), which must also be considered. The net uplift due to design pressure formula from Table 5.21b Addendum 2in API 650 (API, 2013).

Stiffeners: By definition, ring stiffeners are local stiffening members that pass around the circumference of the shell of revolution at a given point on the meridian. Normally they are attached to the interior of the shell of the tank and are formed as single plated sections WT, C or L profiles. The rings are assumed to have limited stiffness for deformations out of their own plane (meridional displacements of the shell) but they should be stiff for deformations in the plane of the ring.(Baniotopoulos et al 2008). According the API 650 (API, 2013); the maximum spacing of intermediate stiffeners

$$H_{safe} = \frac{(ts_{min})^{2.5}(E)}{45,609D^{1.5}(P_S)}$$

the number of intermediate stiffeners required, Ns, based on, H $_{safe.}$

$$Ns + 1 = H_{TS} / H_{safe}$$

and the spacing of intermediate stiffeners on the transformed shell height in accordance with the following equation:

$$\text{Spacing} = H_{TS} / (N_S + 1)$$

Where ts $_{min}$ is minimum thickness of thinnest shell course, mm, E is modulus of elasticity of the plate material MPa, D is nominal tank diameter, m, P_S is total design external pressure for design of shell, kPa (lb/ft^2).Ps = the greater of 1) the specified design external pressure, P_e, excluding wind or 2) w + 0.4P_e

Analysis and design of liquid storage tank using ANSYS.

The development of this research was carried out by the construction of numerical modeling of the tank with help of the computer program ANSYS 17.2. The three-dimensional FE model of self-supporting dome tank was modeled as surfaces using

the pre-processor section in ANSYS. The selection of a suitable element for a given application is not a trivial matter and will directly influence the computational time and accuracy of the results. FE models developed for this study consider the tank wall and base system to be represented and modeled by solid shell element.

DESIGN EXAMPLE --- SELF-SUPPORTING DOME TANK

Geometry, loading and material properties

The specific tank considered in this section is shown in Figure 1 with inner diameter D = 20 m and high of the tank (liquid level) H = 12 m. The design input data is listed in Table 1. The tank is designed for five different courses (2, 3, 4, 5 and 6 courses) and the results are compared for best solution. The courses have equal high. The tank is subjected to hydrostatic loading of a liquid of weight per unit volume and external pressure on the shell wall. The tank is only supported from bottom plate which is fixed support.
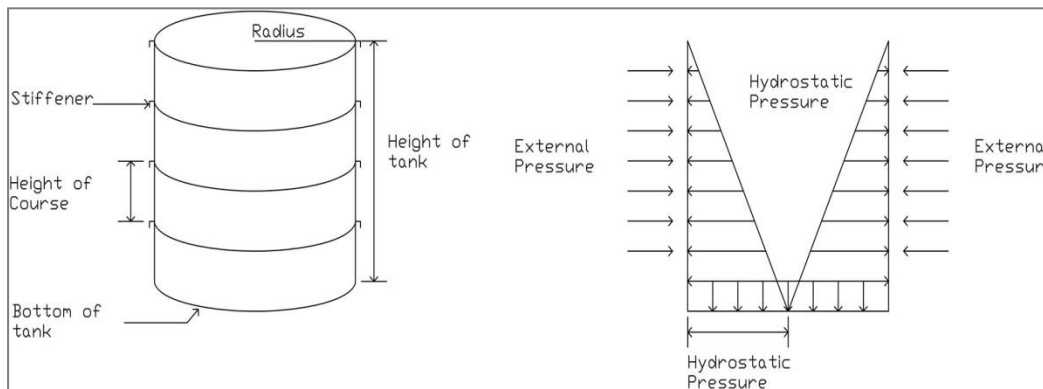
Figure 1 Geometry and loading of tank

Table 1 Design input data

Shell Data			Material Data	
Roof type	Self-supporting dome		Material	A36　M Grade
Density of contents	988.2 kg/m³		Material Group	Group 1
External pressure	3 kPa		Min. Yield Strength	250 MPa
Hydrostatic load	ρgh =0.11633		Min. Tensile Strength	400 MPa
Max. Design Temperature	60 Cº		Modulus of Elasticity	200000 MPa
High liquid level	12 m		Density	7850 kg m³
Basic Wind Speed	190 km/h		Passion's	0.3
Live load	1.5 kN/m²			

Design of tank based on API 650 standard.

The 1-foot method is used to compute the thickness of each courses. Each courses are equal height. Lap welded bottom plates is used and thickness is computed according

to API 650 Section 5.4. There is a wind girder at the top in order to restraint displacements in the upper part of the tank. This is one of the typical stiffening ring sections for tank shells illustrated in API 650 (see details in Figure 5.24 of API 650 (API, 2013)). The number, locations and dimensions of intermediate stiffeners and dimensions of the top wind girder are computed according to API 650 Section 5.9 (API, 2013). The details of the designed tank (according to API 650) are given in Table 2. The thickness of the bottom plate for all courses cases is 9 mm

FE analysis of the liquid storage tank

The FE package ANSYS is employed to carry out the analyses. The 8-node, connectivity, first-order interpolation, stress/displacement continuum solid shell 190 element with reduced integration is chosen to discretize the cylindrical wall. This element has three degrees of freedom at each node: translations in the nodal x, y, and z directions Thus, connecting SOLSH190 with other continuum elements requires no extra efforts. A degenerate prism option is available, but should only be used as filler elements in mesh generation. The element has plasticity, hyper elasticity, stress stiffening, creep, large deflection, and large strain capabilities. It also has mixed u-P formulation capability for simulating deformations of nearly incompressible elastoplastic materials, and fully incompressible hyper elastic materials. The element formulation is based on logarithmic strain and true stress measures. And CONTA174 is used to represent contact and sliding between 3-D "target" surfaces (TARGE170) and a deformable surface, defined by this element. The element has the same geometric characteristics as the solid or shell element face with which it is connected. The element is defined by eight nodes (the underlying solid or shell element has midside nodes). It can degenerate to a six-node element depending on the shape of the underlying solid or shell elements (Canonsburg, 2013).

Table 2. The summary of tank design according to API 650

Number of Course	Thickness of courses (mm)	Number of intermediate Stiffener	Inertia of stiffener (constant stiffener) (cm^4)	Inertia of stiffeners (cm^4)	Location of stiffener from the top (mm)
2	11	1	$I_{1,top}$=224	I_{top}= 220.14	12000
	11			I_1=468.84	6390
3	10	1	$I_{1,top}$=176	I_{top}= 173.36	12000
	10				
	11			I_1= 468.84	5030
4	9	2	$I_{1,2,top}$=176	I_{top}= 173.36	12000
	9				
	9			I_1= 223.56	3870
	11			I_2= 223.56	
5	8	3	$I_{1,2,3,top}$=142	I_{top}= 140.09	12000
	8				
	8			I_1= 134.58	2880
	9			I_2= 134.58	5760

	11			I_3= 180.66	9130
6	7	4	$I_{1,2,3,4,top}$=97.20	I_{top}= 140.09	12000
	7				
	7			I_1= 96.38	2060
	8			I_2= 96.38	4210
	9			I_3= 134.58	6250
	11			I_4= 298.35	10120

For stiffener, three type of profiles (see Figure 2) which have section details satisfying the inertia requirement stated in Table 2 are investigated. The tank is analyzed for following cases:

Case 1: without stiffener
Case 2: constant stiffener (unequal L angle with right orientation)
Case 3: variable stiffener (unequal L angle with right orientation)
Case 4: variable stiffener (unequal L angle with left orientation)
Case 5: variable stiffener (C section)
Case 6: variable stiffener (WT-section)

Case 1 which is tank without stiffener is considered in order to investigate the effect of stiffener. Case 1 does not satisfy the API 650 standards. In the case of constant stiffener, the minimum inertia value which is computed according to API 650 is used in all stiffener. In case of variable stiffener, the inertia of each stiffener is computed individually according to API 650. In this case, C, Unequal L angle with two different orientations and WT profile sections are investigated. In order to get meaningful comparison, the inertial values of different types of profiles are selected from catalogue in a way that they approximately equal to each other.
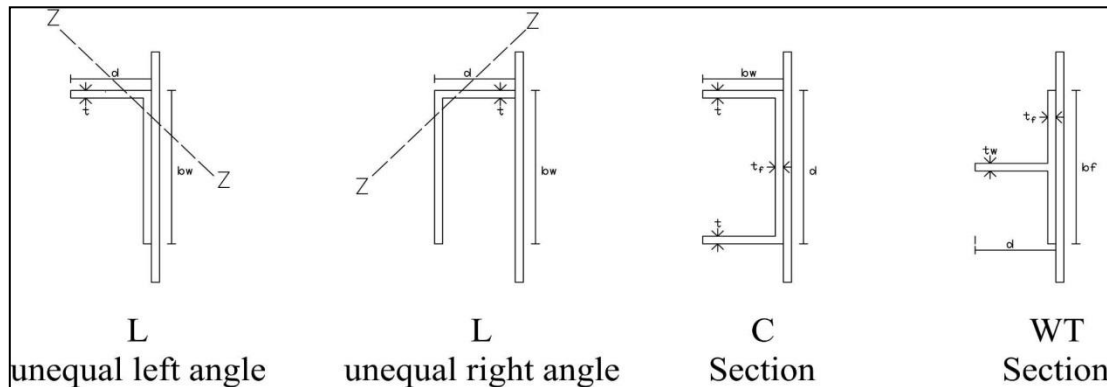
Figure 2 Type of stiffener profiles

The linear static, free vibration and buckling analyses are carried out using ANSYS commercial software for the designed tank according to API 650 standard. The tanks are modelled and analyzed using fine meshes. The FE model of the tank is shown in Figure 3. The stress distribution and deformations in the tanks and weight, fundamental frequency and critical buckling loads of tanks are observed. The effect of the number of course, stiffener, location of stiffener, type of stiffener is investigated.
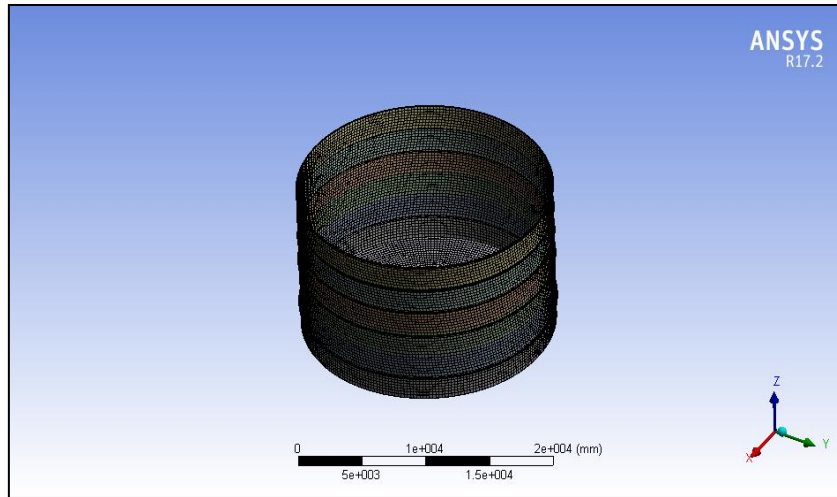
Figure 3 FE model of tank

RESULT AND DISCUSSION

The results of finite element analyses for static, free vibration and buckling is summarized in Table 3. The maximum equivalent stresses are very close to each other for all cases considered. The maximum equivalent stress is occurred at Case 5 with 6 courses and equal to 112.75 MPa which is less than minimum yield stress 250 MPa. The stress distribution for this tank is shown in Figure.4.

Table 3 The result of finite element analysis.

	Courses	Case 1	Case 2	Case 3	Case 4	Case 5	Case 6
Max.von Mises Stress (MPa)	2	110.36	110.37	110.01	110.88	111.16	111.25
	3	110.36	110.38	110.38	110.31	111.19	110.3
	4	110.20	110.22	110.23	110.24	110.21	110.22
	5	111.73	111.74	111.75	111.74	111.74	111.71
	6	110.77	110.08	110.76	110.96	112.75	111.42
Max. Deformation (mm)	2	5.20	5.20	5.25	5.27	5.30	5.28
	3	5.22	5.22	5.22	5.22	5.28	5.22
	4	5.28	5.29	5.29	5.29	5.29	5.28
	5	5.32	5.32	5.32	5.32	5.31	5.32
	6	5.41	5.27	5.45	5.31	5.32	5.41
Fundamental Frequency (Hz)	2	6.4982	8.0534	8.1817	13.511	14.983	15.082
	3	6.7285	8.0357	8.3399	11.833	10.997	15.295
	4	6.9648	8.8812	8.8492	13.086	12.976	11.694
	5	7.2738	9.1952	9.1938	15.739	12.186	19.757
	6	7.6199	9.6296	9.5513	17.213	21.189	20.899
Buckling Multiplier	2	-1.1489	-1.2169	-1.2177	-1.2285	-1.2325	-1.2267
	3	-1.1244	-1.1738	-1.1748	-1.1793	-1.1813	-1.1813
	4	-1.0964	-1.2470	-1.2455	-1.2624	-1.2727	-1.2712
	5	-1.0772	-1.2434	-1.2443	-1.2823	-1.3107	-1.2832
	6	-1.0595	-1.1932	-1.1888	-1.2109	-1.2394	-1.2089
Weight	2	87386.00	88722.28	89024.05	89024.05	91959.11	88966.52
	3	83440.00	85154.74	85212.55	85212.55	87293.65	84643.26
	4	78499.00	81876.13	81593.72	81593.72	83589.10	83491.31
	5	74352.40	77037.52	77254.83	77254.83	84170.40	76992.84
	6	70600.70	73697.67	74101.41	74101.41	82191.12	73702.55
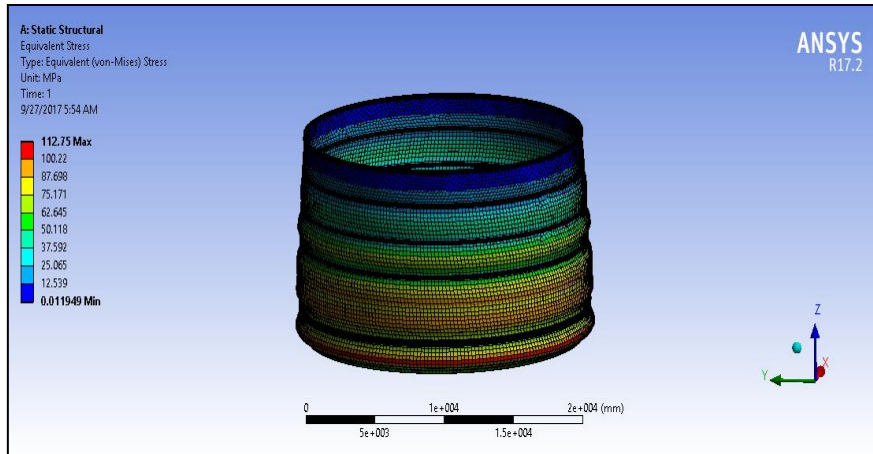
Figure 4 The maximum equivalent stresses

The maximum deformations are again very close to each other for all cases considered. The maximum deformation is occurred at Case 3 with 6 courses and equal to 5.45 mm. The deformation for this tank is shown in Figure 5.
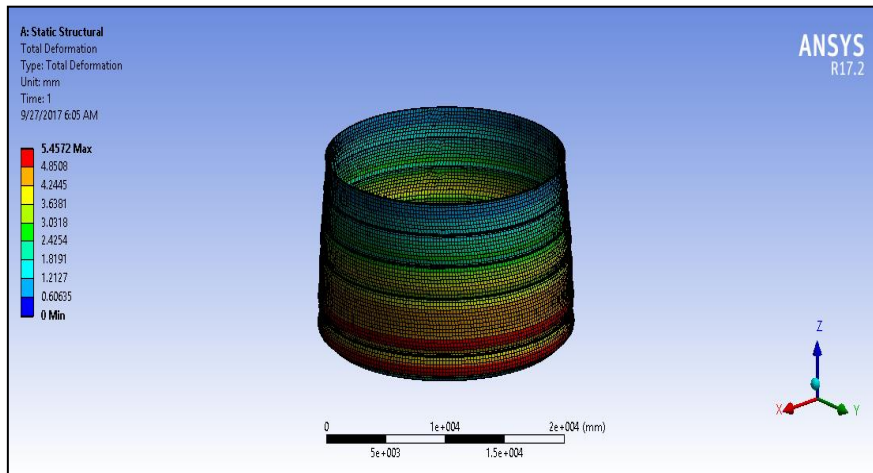
Figure 5 The maximum deformations

The one of the main reason of failure of tank is buckling. The buckling analyses of the tank are carried out and the buckling multiplier are computed and presented in Table 3. The worst case is the tank without stiffener. The best solution against buckling is obtained in Case 5 where C section stiffener is used. The maximum buckling multiplier is occurred at Case 5 with 5 courses and equal to -1.3107. The corresponding buckling mode shape is shown in Figure 6.
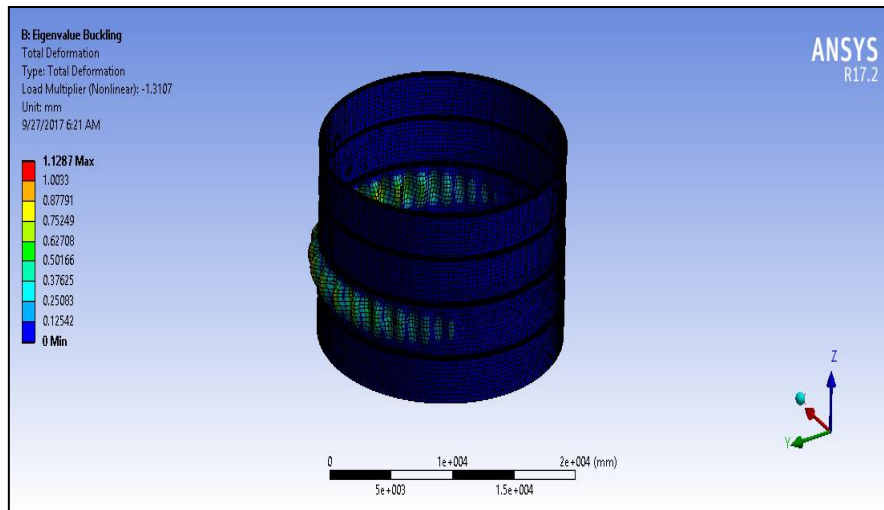
Figure 6 The maximum buckling multiplier

The seismic behavior of the tanks is investigated by studying fundamental frequency. The maximum fundamental frequency is occurred at Case 5 with 6 courses where C section stiffener is used and equal to 21.189mm. The corresponding mode shape is shown in Figure 8. The lowest fundamental frequencies are obtained in Case 1 as expected.

The weight of the tanks decrease with increasing number of courses. The lightest tank is obtained in case of without stiffener. The heaviest tanks are found in case of C section stiffeners.

CONCLUSIONS

In this paper the preliminary design of elements of a circular liquid tank by the API was performed. With obtained dimensions of elements, tank was modeled in the software package ANSYS, and values of maximum stresses and deformation were computed and compared. The stiffeners improve the static, buckling and dynamic behavior of the tank WT and C section stiffener show better performance. When the number of the courses increase the weight of the tank is reduced meanwhile the structural behavior of the tank does not change so much.
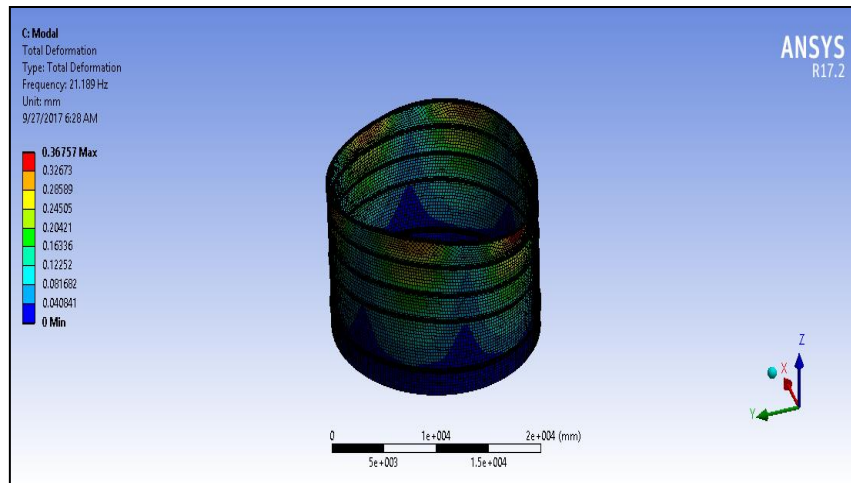
Figure 7 The maximum fundamental frequency

REFERENCES

American Petroleum Institute. (2002). API 620: Design and Construction of Large, Welded, Low Pressure Storage Tanks, 552(3), 1–194.

American Petroleum Institute. API. (2013). Welded Tanks for oil Storage API 650, (March), 498.

Baniotopoulos, C., Lavasas, I., Nikolaides, G., & Zervas, P. (2008). RFS-CT-2006-00031 - HISTWIN High-Strength Steel Tower for Wind Turbine.

British Standards Institution (BSI). (2004). BS EN 14015:2004: Specification for the design and manufacture of site built , vertical , cylindrical , flat-bottomed , above tanks for the storage of liquids at ambient temperature and above. Standards, 3(1).

Burgos, C. A., Batista-Abreu, J. C., Calabr, H. D., Jaca, R. C., & Godoy, L. A. (2015). Buckling estimates for oil storage tanks: Effect of simplified modeling of the roof and wind girder. Thin-Walled Structures, 91, 29–37. https://doi.org/10.1016/j.tws.2015.02.006

Canonsburg, T. D. (2013a). ANSYS Mechanical APDL Element Reference, 15317(November), 724–746.

Canonsburg, T. D. (2013b). ANSYS Mechanical Users Guide, 15317(November), 724–746.

Cao, Q. shuai, & Zhao, Y. (2010). Buckling strength of cylindrical steel tanks under harmonic settlement. Thin-Walled Structures, 48(6), 391–400. https://doi.org/10.1016/j.tws.2010.01.011

Chauhan, Mukeshm.(2012). Design and stability of large storage tanks and tall bins, (803), 1–48.

Elkholy, S. A., Elsayed, A. A., & Sadek, S. A. (2014). Optimal finite element modelling for modal analysis of liquid storage circular tanks Bilal El-Ariss, 5(3), 207–241.

Y.G. Fakhım, H. Showkatı , K. Abedı (2009) Experimental study on the buckling and post- buckling behavior of thin-walled cylindrical shells with varying thickness under hydrostatic pressure . (January).

Mayeux, S., & Miller, J. (2016). Designing storage tanks.

george w. housner. (1963). The dynamic behavior of water tanks, bulletin of the Seismological Society of America , 53(2), 381–387.

Spritzer, J. M., & Guzey, S. (2017). Review of API 650 Annex E: Design of large steel welded aboveground storage tanks excited by seismic loads. Thin-Walled Structures, 112(September 2016), 41–65. https://doi.org/10.1016/j.tws.2016.11.013

REHABILITATION OF HIGH STRENGTH REINFORCED CONCRETE CORBELS USING BASALT FIBER FABRIC

Adnan Hazem Alshawaf
Gaziantep University, Civil Engineering Department
eng_shawaf@hotmail.com

Mehmet Eren GÜLŞAN
Gaziantep University, Civil Engineering Department
gulsan@gantep.edu.tr

Khamees Nayyef Abdulhaleem
Gaziantep University, Civil Engineering Department
khamees.abdulhaleem@mail2.gantep.edu.tr

ABSTRACT: This paper presents an experimental study on the mechanical behavior of damaged reinforced concrete corbels rehabilitated by Basalt Fiber Fabric (BFF). The main research aim of the study is to investigate the effectiveness of basalt fiber fabric on rehabilitation of reinforced concrete corbels, which were damaged because of elevated temperatures and overloading, by examining load restoring capacity and ductility. Totally nine corbels that had been damaged before were selected for the study. The initial failure of the corbels had been because of overloading after heating them to several temperature levels (250ᵒC, 500ᵒC, and 750ᵒC). These corbels had been produced from high strength self-compacting concrete with one concrete class (80 MPa) and three different amounts of steel fiber ratios (0%, 0.5%, 1%). However, shear span value for all corbels is same (90 mm). Experimental results show that use of basalt fiber fabric on damaged corbels increases the load carrying capacity and ductility significantly as compared to the corresponding values of corbels before initial failure. Besides, the stiffness of the corbels after rehabilitation is same with the stiffness of them before initial failure. Moreover, all of the rehabilitated corbels failed because of de-bonding failure mode and no visible damage was observed on the fabric.

Key words: corbels, high strength concrete, rehabilitation, basalt fiber fabric, epoxy.

INTRODUCTION

Corbels are short cantilever deep beam with a shear span, structural members commonly used in reinforced concrete and Precast concrete structures. As known, the corbels are widely used in industrial buildings and highway bridges. The main function for the corbels are transferring the vertical and horizontal loads between members such as the beams to columns and walls (Foster & Malik, 2002; Foster, Powell, & Selim, 1996; Hwang & Lee, 2002; Russo, Venir, Pauletta, & Somma, 2006; Yong & Balaguru, 1994) . The strength and stiffness for reinforced concrete corbels could be affected if the corbels are exposed to heat treating. Previous experimental

studies concrete behavior under high temperatures have mostly focused on the reduction of stiffness and strength properties(Toumi, Resheidat, Guemmadi, & Chabil, 2009). In order to maintain the structural members form degradation or loss the main function for this member, the researchers were investigated rehabilitation methods and a mechanism to maintain those members. However, many reasons demand to rehabilitate concrete structures not just heat treatment such as, use consideration (change in loading requirements), environmental conditions, construction and material shortcomings (incorrect placing of steel bars, redesign the members, inadequate lap length at splice or inadequate transversal reinforcement like; hoops, ties, or stirrups, and weak constructions practice(Elgwady, Rabié, & Mostafa, 2005) . As well as, structural rehabilitation's is play a role in civil engineering, to rectify damaged, corroded and old reinforcement concrete structures in common terms likewise repairing, rehabilitating and strengthening with this in mind processes related to damage ratio(Kumar, Selvamony, Seeni, & Sethuraman, 2015). The variation in rehabilitate and other methods for repairing reinforcement concrete isn't so much obvious, because a lot of reason may cause failure in concrete such as overloading. On other circumstance, crack observed in the concrete so if the corbels is undamaged and the structure live load is to be increased, then the appliance is merely for strengthening functions (Corry & Dolan, 2001). While The most important factors for using composite materials is strengthening the structure. To give an illustration, the data elucidate repair or strengthening techniques for reinforced concrete corbels by Basalt fiber fabric are very limited and almost nonexistent, another key thing to remember many researchers investigates on basalt fiber reinforced polymer composites ,the study confirm when basalt fiber had been used the fracture toughness increases as a result of reinforcing , the toughness of the composite increased compared to the matrix (BFP) and loading capacity(Czigány, Vad, & Pölöskei, 2005; Kumar et al., 2015; Liu, Shaw, Parnas, & McDonnell, 2006) . Moreover, on other hand researchers investigates strengthening on reinforced concrete corbels by utilizing carbon fiber (CFRP) and they found by using CFRP technology for strengthening and repairing reinforced concrete corbels was operative and efficient too(Ahmad, Elahi, Kundi, & Haq, 2013; Erfan, Abdel-Rahman, Nassif, & Hammad, 2010; I Ivanova & Assih, 2015; Ivelina Ivanova & Assih, 2015; Ivelina Ivanova, Assih, & Dontchev, 2016) .

This paper presents results of an investigation on the experimental behavior of heated and damaged steel fiber Reinforced corbels after rehabilitated using basalt fiber fabric and to Figure out the change between the ultimate load and the failure mode after the rehabilitation.

EXPERIMENTAL WORK

The experimental study consists of nine corbels. All of the damaged corbels had been produced from self-compacting high-strength steel fiber reinforced concrete (compressive strength value of 80 MPa). While all corbels have the same shear span ratio (0.69) and reinforcement ratio (0.0158), they contain different amount of steel

fiber (0%, 0.5%, and 1%). Moreover, all corbels had been damaged before rehabilitation process because of overloading after different heating levels (temperature values of 250°C, 500°C, and 750°C). After the damaged corbels were rehabilitated by basalt fiber fabric, they were reloaded until failure. All details about the rehabilitation of corbels and testing procedure are explained in the following parts.

Corbel details

All corbels have the same geometry and steel reinforcement arrangement which are shown in Fig. 1. The cross-section dimensions of both column and corbels are 150mm x 150mm. Column part of the column had been reinforced with four 10 mm diameter steel bars for longitudinal reinforcement and of four 8 mm diameter steel bars for stirrups. Besides, two 14 mm diameter deformed steel bars were used for the main reinforcement of all corbels and the concrete cover distance for all corbels is 20 mm. All corbels were supported by roller supports during loading tests.
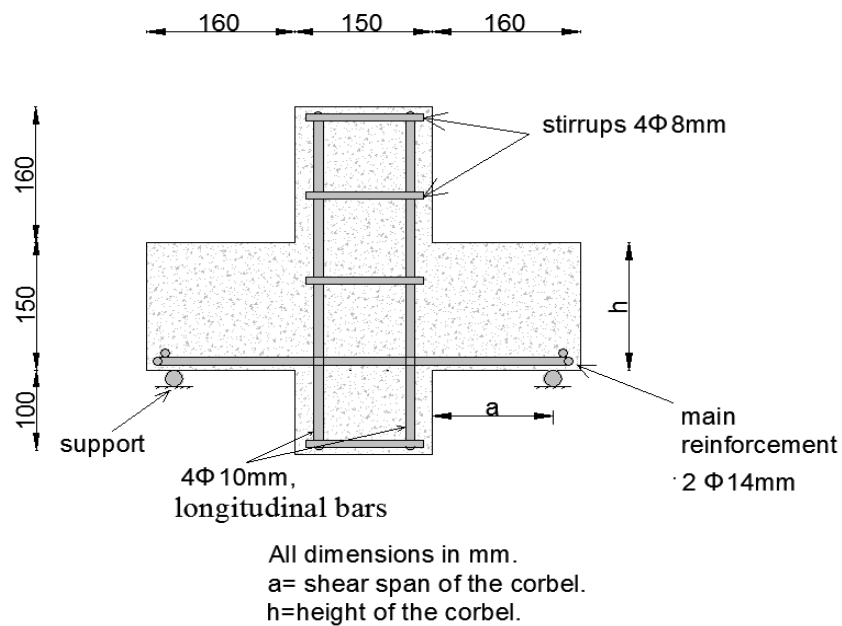
Figure 1. Corbel detail

Materials properties

In this experimental study, three types of epoxy were used. Each one was preferred for a different purpose in the rehabilitation process. High viscosity epoxy adhesive (TEKNOBOND 200) was used both for the repair of damaged concrete parts and for closing the cracks on the corbel surface in order to prevent leakage of crack repair material. Low viscosity epoxy adhesive (TEKNOBOND 300 TIX) was used for gluing the basalt fiber fabric to the concrete surface. The mechanical and physical properties of the high and low viscosity epoxy adhesives are shown in Table 1.

Table 1. The properties of high and low viscosity epoxy adhesive

Density (gr/cm3)	Consumption (kg/m)	Bond to Concrete (N/mm2)	Pot Life (min)	Loading capability (day)	Full strength (day)	Application Ground Temperature (°C)
low viscosity epoxy	1.15 A 1.05 B 2	5.3	45	1	7	5-30
high viscosity epoxy	1.50 1.5	4	30	1	7	5-30

The third type of epoxy was very low viscosity injection resin (Sikadur-52) which was used as crack repair material. It was injected to the inner micro cracks in as much of his flowability in order to close all cracks both inside the corbels and on the corbel surface. The properties of this epoxy are shown in Table 2.

Table 2. The properties of very low viscosity injection resin

Density (kg/l)	Compressive Strength (N/mm²)	Bond to Concrete (N/mm²)	Pot Life (min)	Flexural Strength (N/mm²)	Tensile Strength (N/mm²)	E-Modulus (N/mm²)
1.1 A 1 B	52	4	25	61	37	1800

The most important material of the study is basalt fiber fabric (BFF). Unidirectional basalt fiber fabric was treated for the rehabilitation of the damaged corbels. Reasons for the selection of this fabric type can be listed as a high tensile strength, smooth texture, durability, fire resistance and cheapness as compared to other alternatives (such as carbon fiber fabric). The properties of the fabric are shown in Table 3.

Table 3. The properties of basalt fiber fabric

Tensile Strength (MPa)	Tensile Modulus of Elasticity (Gpa)	Elongation (0/0)	Thickness (mm)	Polyester Yarn Density (tex)	Area Weight (g/m2)
2100	105	2.6	.115	5.25	300

Rehabilitation methods

The grinder machine was used to clean the surfaces of corbels. The top four corners were rounded to achieve the continuity in the rehabilitated system, to prevent stress concentrations and to avoid tearing in basalt fabric. Before the gluing operation, the

air compressor was used to remove any loose particles or dust on the surface. High viscosity epoxy adhesive was used for closing the big cracks in order to prevent the leakage of very low viscosity crack repair epoxy and to substitute the loosing parts of the damaged corbels. Thereafter, the cracks and voids were filled out with very low viscosity crack repair epoxy. The repair epoxy was injected to the inner of corbels by small injection needles and gravity feed method was used for the injection process. After injection process, the corbels were left for seven days to achieve the target strength of the repair epoxy. Application of the first part of the rehabilitation process in order to repair the cracks is shown in Fig. 2 step by step.
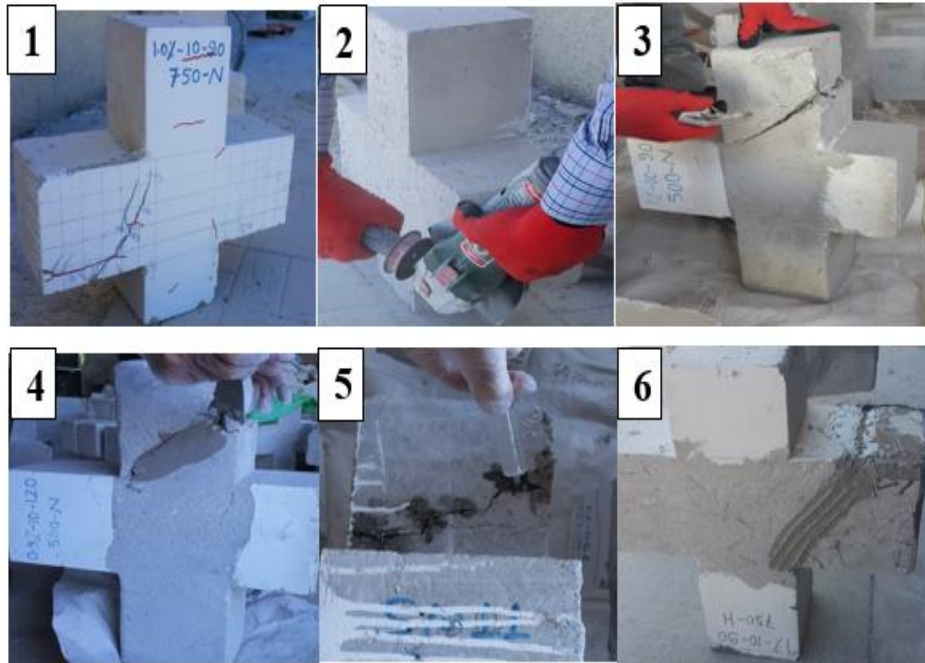
Figure 2. Configuration steps of preparation surface and injecting with very low viscosity injection

In the second part of the process, three strips of basalt fiber fabric were cut in specific dimensions for all corbel specimens. Components of low viscosity epoxy (epoxy and hardening resin) are mixed by electric drill machine according to low viscosity epoxy adhesive product data sheet. Thereafter basalt fiber fabric was saturated with the low viscosity epoxy and the saturated fabrics were glued to the corbel surface. The fabric was glued to the surface according to the shape and geometry of the corbels. Moreover, escaping from the voids is very important during gluing process. Therefore, trowel was used to eliminate air voids and to achieve successful connection between the fabric and the surface. Since basalt fiber fabric is unidirectional, it was glued to the corbel surface in both vertical and horizontal directions in order to resist normal stresses existing in both directions. Lastly, grinder machine was used again to level bottom of corbels in order to achieve smooth and homogeneous load transfer mechanism during loading. Step by step implementation of the second part of the rehabilitation process is shown in Fig. 3.
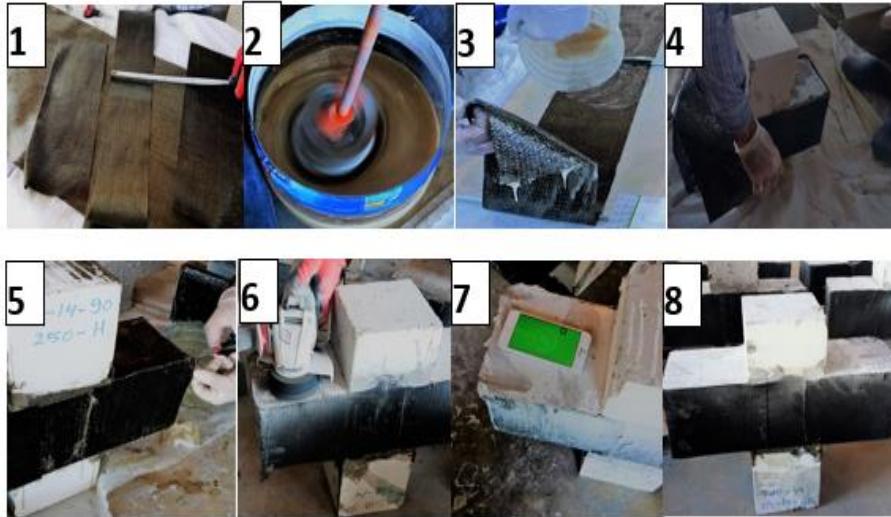
Figure 3. Configuration steps of the bonding surface and applying the Basalt fiber fabric with epoxy

Test Setup

All corbels were tested before and after the rehabilitation process under three-point loading tests Figure 4. Tests were carried out via 500 kN capacity displacement-controlled loading machine. The corbels were loaded with rate of 0.3 mm/min. Deflection of corbels was measured by two linear-variable-displacement-transducers (LVTDs). Load and displacement values were recorded at every 0.2seconds.

Figure 4. Corbel Specimen Setup

EXPERIMENTAL RESULTS AND DISCUSSION

Loading test results with all details are shown in Table 4. The first column in the table names designation for the corbels, including all related values, in which six different terms are provided for each corbel's name; the first term represents the

number of the specimen and the remain terms represent compressive strength, steel fiber ratio, main bar diameter, degree of heating before initial failure, and shear span length, respectively. As a result of tests, it was concluded that load capacity of the high strength reinforced concrete corbels increased an amount of 50% averagely as compared to the corresponding values before rehabilitation. Moreover, strengthening with basalt fiber fabric enhanced the ductility of corbels noticeably. Therefore, a preferable seismic performance of reinforced concrete corbels can be achieved with basalt fiber fabric even they are damaged due to both fire and overloading. Besides, the failure modes of the corbels before and after rehabilitation are summarized in Table 4. All of the corbels have the same failure pattern after repairing which is debonding between the basalt fiber fabric and the surface of corbels as shown in Fig. 5. Even different failure modes had been observed in the initial failure of the corbels, failure modes of all corbels after rehabilitation were debonding failure. This result can be attributed to the placement of the fabric in two directions which makes the fabric much more powerful leading to prevention of the tearing of the fabric.

Table. 4 Details of rehabilitated corbels

Name	Max. Carrying load before Rehabilitation PU (KN)	Max. Carrying load After Rehabilitation *PU (KN)	*PU/PU	Max. Deflection(mm) At Failure Load (Before the Rehabilitation)	Max. Deflection(mm) At Failure Load (After the Rehabilitation)	Mode of failure before the Rehabilitation	Mode of failure after the Rehabilitation
C0-80-0.0-14-250-90	268	292.5	1.09	0.744	4.443	Shear failure	De-bonding
C1-80-0.0-14-500-90	210	246.5	1.17	1.654	3.60	Diagonal splitting	De-bonding
C2-80-0.0-14-750-90	113	150	1.32	1.231	7.583	Shear failure	De-bonding

Table 4 Details of rehabilitated corbels (Continued)

C3-80-0.5-14-250-90	370	399.6	1.08	1.60	7.3	Shear failure	De-bonding
C4-80-0.5-14-500-90	251	262	1.04	2.309	6.292	Shear failure	De-bonding
C5-80-0.5-14-750-90	134	201	1.50	1.654	3.69	Shear failure	De-bonding
C6-80-1.0-14-250-90	382	430.3	1.13	2.048	6.125	Shear failure	De-bonding
C7-80-1.0-14-500-90	294	306	1.04	2.329	3.805	Shear failure	De-bonding
C8-80-1.0-14-750-90	183	187.5	1.02	1.68	6.886	Shear failure	De-bonding

Figure 5. Specimen with De-bonding failure

Figure 6 shows the Load-Deflection relationships that came from testing of injected corbels.
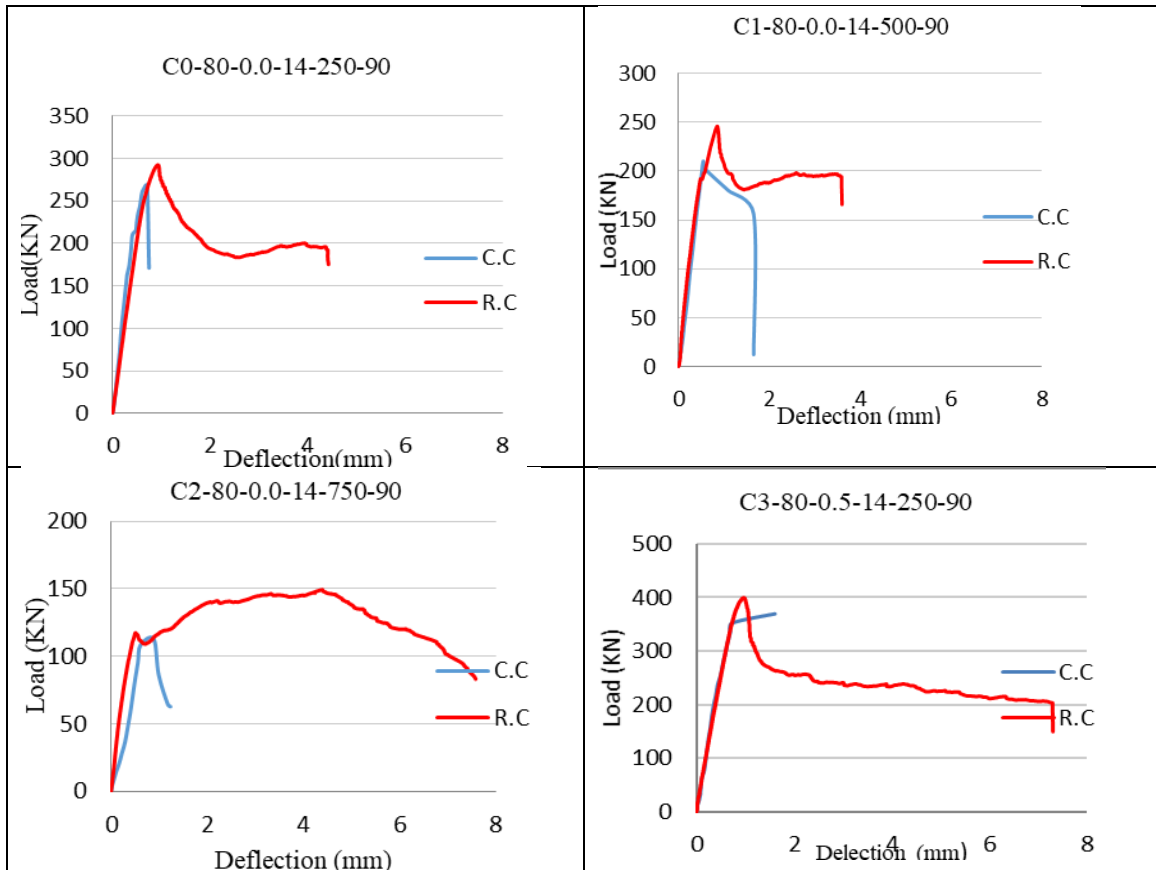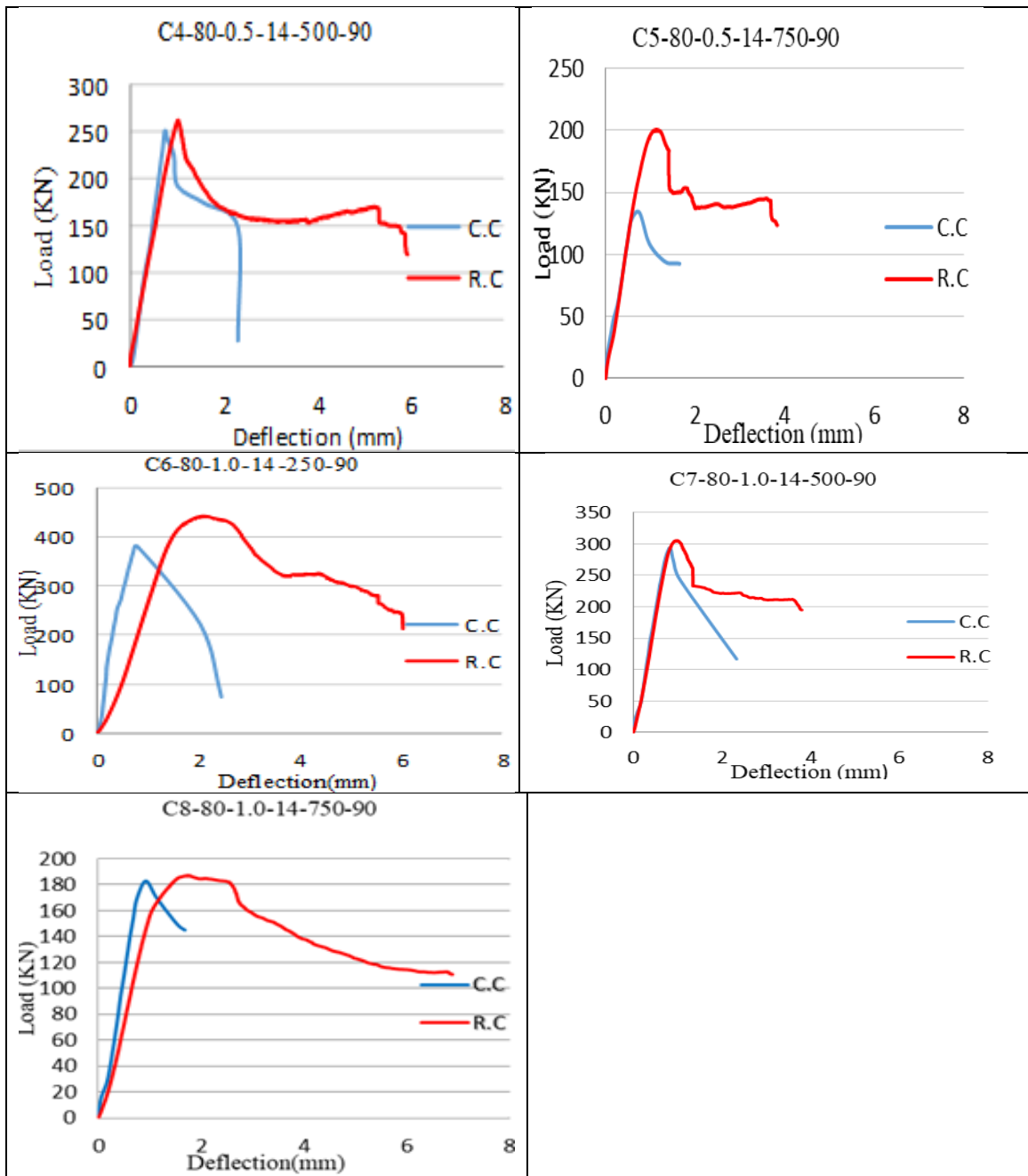
Figure 6 Load-deflection curves of rehabilitated corbels

CONCLUSION

In this study, a new technique was investigated for the rehabilitation of damaged reinforced concrete corbels reinforced with or without steel fiber for the first time in literature. Damaged corbels due to exposure to high temperature and overloading were repaired by crack repair epoxy and strengthened by basalt fiber fabric (BFF). The effectiveness of the method was researched by vertical loading tests. In general, it is concluded that use of crack repair epoxy and basalt fiber fabric for the rehabilitation of damaged reinforced or steel fiber reinforced concrete corbels increases the original load capacity and ductility considerably.

The following conclusion can be estimated after the experimental study:
In general, rehabilitation with basalt fiber fabric increases the load capacity of corbels and it ensures restoring original load capacity of the corbels. Energy absorption capability and ductility for all the BFF-strengthened corbels increases. The existence of steel fiber plays an important role in the rehabilitation of high strength concrete corbels about ductility. It increases the effectiveness of the rehabilitation due to partial restoring of bridging effect of steel fibers. This situation leads to an economical solution for rehabilitation of corbels by using BFF. As a result of the study, it is also concluded that almost the same stiffness value of corbels before rehabilitation is achieved after rehabilitation of them with basalt fiber fabric. Moreover, the existence of a high number of micro and macro cracks in damaged corbels decreases the effectiveness of the proposed rehabilitation technique, especially an increase in the load capacity of them.

RECOMMENDATIONS

As compared to the alternatives, basalt fiber fabric is one of the most economical and effective technique for the rehabilitation of reinforced concrete high strength corbels. The authors recommend that either use of bi-directional basalt fiber fabric or use of uni-directional fabric in two directions (horizontal and vertical) makes the proposed rehabilitation technique much more effective.
This study can be extended by the investigation of more economical solutions about the rehabilitation of damaged corbels. For instance, basalt fiber fabric can be cut into thin strips and these strips can be glued to the critical regions of the damaged corbels in which higher stresses and wider cracks were expected due to vertical loading.

REFERENCES

Ahmad, S., Elahi, A., Kundi, S., & Haq, W. (2013). Investigation of shear behavior of Corbel beams strengthened with CFRP. Life Science Journal, 10(12s). article.
Corry, R. W., & Dolan, C. W. (2001). Strengthening and repair of a column bracket using a carbon fiber reinforced polymer (CFRP) fabric. PCI Journal, 46(1).

Czigány, T., Vad, J., & Pölöskei, K. (2005). Basalt fiber as a reinforcement of polymer composites. Periodica Polytechnica. Engineering. Mechanical Engineering, 49(1), 3.

Elgwady, M. A., Rabié, M., & Mostafa, M. T. (2005). Strengthening of corbels using CFRP an experimental program. Cairo University, Giza, Egypt.

Erfan, A. M., Abdel-Rahman, G. T., Nassif, M. K., & Hammad, Y. H. (2010). Behavior of reinforced concrete corbels strengthened with CFRP fabrics. Benha University. article.

Foster, S. J., & Malik, A. R. (2002). Evaluation of efficiency factor models used in strut-and-tie modeling of nonflexural members. Journal of Structural Engineering, 128(5), 569–577.

Foster, S. J., Powell, R. E., & Selim, H. S. (1996). Performance of high-strength concrete corbels. ACI Structural Journal, 93(5), 555–563.

Hwang, S.-J., & Lee, H.-J. (2002). Strength prediction for discontinuity regions by softened strut-and-tie model. Journal of Structural Engineering, 128(12), 1519–1526.

Ivanova, I., & Assih, J. (2015). EXPERIMENTAL STUDY OF LOCAL BEHAVIOR OF STRENGTHENED REINFORCED CONCRETE SHORT CORBEL BY BONDING CARBON FIBER FABRICS. article.

Ivanova, I., & Assih, J. (2015). Static and dynamic experimental study of strengthened inforced short concrete corbel by using carbon fabrics, crack path in shear zone. Frattura Ed Integrita Strutturale, (34). article.

Ivanova, I., Assih, J., & Dontchev, D. (2016). Mechanical Pathologies of Reinforced and Damaged Concrete Corbels by Gluing Composite Carbon Fabrics Under Static and Dynamic Tests. In Sustainable Construction (pp. 185–211). incollection, Springer.

Kumar, R. A., Selvamony, C., Seeni, A., & Sethuraman, T. R. (2015). Retrofitting Of RCC Piles By Using Basalt Fiber Reinforced Polymer (BFRP) Composite, Part: 1 Review Papers On RCC Structures And Piles Retrofitting Works. International Journal of Technology Enhancements and Emerging Engineering Research, 4(1), 103–115. article.

Liu, Q., Shaw, M. T., Parnas, R. S., & McDonnell, A.-M. (2006). Investigation of basalt fiber composite mechanical properties for applications in transportation. Polymer Composites, 27(1), 41–48.

Russo, G., Venir, R., Pauletta, M., & Somma, G. (2006). Reinforced concrete corbels-shear strength model and design formula. ACI Structural Journal, 103(1), 3.

Toumi, B., Resheidat, M., Guemmadi, Z., & Chabil, H. (2009). Coupled Effect of High Temperature and Heating Time on the Residual Strength of Normal and High-Strength Concretes. Jordan Journal of Civil Engineering, 3(4), 322–330.

Yong, Y.-K., & Balaguru, P. (1994). Behavior of reinforced high-strength-concrete corbels. Journal of Structural Engineering, 120(4), 1182–1201.